

Measurement of Elliptic Flow Coefficients and Derivation of Reaction Plane Dependent  
Efficiency of Isolated Photons and  $\pi^0$  Mesons in  $\sqrt{s_{NN}} = 200$  GeV Au+Au Collisions at  
**RHIC-PHENIX**

A thesis presented to  
the faculty of  
the College of Arts and Sciences of Ohio University

In partial fulfillment  
of the requirements for the degree  
Master of Science

Tyler Danley  
December 2014  
© 2014 Tyler Danley. All Rights Reserved.

This thesis titled

Measurement of Elliptic Flow Coefficients and Derivation of Reaction Plane Dependent Efficiency of Isolated Photons and  $\pi^0$  Mesons in  $\sqrt{s_{NN}} = 200$  GeV Au+Au Collisions at  
**RHIC-PHENIX**

by

**TYLER DANLEY**

has been approved for

the Department of Physics and Astronomy  
and the College of Arts and Sciences by

Justin Frantz

Assistant Professor of Physics and Astronomy

Robert Frank

Dean, College of Arts and Sciences

## ABSTRACT

DANLEY, TYLER, M.S., December 2014, Physics and Astronomy

---

Measurement of Elliptic Flow Coefficients and Derivation of Reaction Plane Dependent  
 Efficiency of Isolated Photons and  $\pi^0$  Mesons in  $\sqrt{s_{NN}} = 200$  GeV Au+Au Collisions at  
RHIC-PHENIX (79 pp.)

Director of Thesis: Justin Frantz

This thesis presents measurements of second order flow coefficients and derivations of reaction plane dependent efficiencies of isolated photons and  $\pi^0$ 's in  $\sqrt{s_{NN}} = 200$  GeV Au+Au collisions at RHIC-PHENIX. We used an isolation cut method similar to those used in direct photon identification where the energy is summed inside an angular cone and cut if greater than a threshold energy. We show that this will result in a reaction plane dependent efficiency. We derive azimuthal single and two particle correlation functions, including this efficiency, up to harmonic second order. These functions were then verified using a Monte Carlo program.

Measurements were made in four centralities using the typical event plane method. We show that this method is only sensitive to  $v_{2effective}$ , which includes the sum of true  $v_2$  and the  $v_2$  of the isolation efficiency, which is generally negative. Hence, the measurements of  $v_{2effective}$  are generally smaller, even reaching negative values, than those previously observed for photons and  $\pi^0$ 's. A method for measuring the efficiency  $v_2$  is presented, which is required in order to find the true isolated photon and  $\pi^0 v_2$ .

## **ACKNOWLEDGMENTS**

I would like to thank Dr. Justin Frantz for his patience and guidance through this project. I look forward to working with him in the future. I also like to thank my committee members, Dr. David Drabold and Dr. Heather Crawford for taking time out of their schedules at the busiest time of the year to play a role in this MS thesis. Finally, I would like to thank my friends for their infallible support.

## TABLE OF CONTENTS

	Page
Abstract . . . . .	3
Acknowledgments . . . . .	4
List of Tables . . . . .	7
List of Figures . . . . .	8
<b>1 Introduction . . . . .</b>	<b>10</b>
1.1 The Standard Model . . . . .	10
1.1.1 Gauge Bosons . . . . .	10
1.1.2 Quarks . . . . .	11
1.1.3 Leptons . . . . .	12
1.1.4 Quantum Chromodynamics . . . . .	13
1.2 Heavy Ion Collisions . . . . .	16
1.2.1 Event Evolution . . . . .	16
1.2.2 Event Characterization . . . . .	17
1.2.2.1 Centrality . . . . .	17
1.2.2.2 Coordinate Systems . . . . .	18
1.2.2.3 Reaction Planes . . . . .	19
1.2.3 QGP Signatures . . . . .	21
1.2.3.1 Harmonic Flow . . . . .	22
1.2.3.2 Single Particle Suppression . . . . .	23
1.2.3.3 Jet Suppression . . . . .	24
1.3 Flow Coefficient Determination and Systematic Errors . . . . .	27
1.4 Motivation of This Thesis . . . . .	29
<b>2 Experimental Details . . . . .</b>	<b>31</b>
2.1 Relativistic Heavy Ion Collider . . . . .	31
2.2 Pioneering High Energy Nuclear Interaction Experiment . . . . .	32
2.2.1 Beam Beam Counter . . . . .	35
2.2.2 Zero Degree Calorimeter . . . . .	36
2.2.3 Reaction Plane Detector . . . . .	37
2.2.4 Muon Piston Calorimeter . . . . .	38
2.2.5 Electromagnetic Calorimeter . . . . .	38

3	Analysis and Discussion I: Reaction Plane Efficiency and Monte Carlo Simulations	41
3.1	Introduction	41
3.2	Derivation of Reaction Plane Efficiency Trigger distribution	41
3.3	Monte Carlo Confirmation of Reaction Plane Efficiency Trigger distribution	42
3.3.1	Acceptance Correction	43
3.4	Derivation of the Two Particle Correlation Function with Reaction Plane Efficiency	46
3.5	Confirmation of the Isolation Cut Reaction Plane Efficiency	51
3.5.1	Isolation Cut	51
4	Analysis and Discussion II: Measurement of Elliptic Flow Coefficients of Isolated $\gamma$ and $\pi^0$ in PHENIX Run 10	56
4.1	Data Selection	56
4.1.1	Isolation Cut	58
4.1.2	Acceptance Correction	59
4.2	Extracting $v_2$	60
4.2.1	Event Plane Resolution	61
4.3	Measurement of $v_{2\text{effective}}$	62
4.4	Systematic Errors with Resolution Considerations	69
5	Outlook and Conclusions	72
5.1	Isolation Cut Efficiency	72
5.2	Measurement of Higher Order Flow Harmonics	74
5.3	Different Collision Systems	76
5.4	Final Words	76
	References	78

**LIST OF TABLES**

Table	Page
1.1 Fundamental forces and gauge bosons . . . . .	11
1.2 Summary of quarks . . . . .	12
1.3 Summary of leptons . . . . .	13
2.1 PHENIX subdetectors . . . . .	34
2.2 Summary of PHENIX data . . . . .	40
4.1 Isolation cut paramters for all centralities . . . . .	59
4.2 Resolution systematic errors . . . . .	70

## LIST OF FIGURES

Figure	Page
1.1 QCD phase diagram . . . . .	15
1.2 Time evolution of gold collision . . . . .	17
1.3 Two centralities with impact parameters. . . . .	18
1.4 Collision cartoons for just elliptic flow and higher order flow harmonics. . . . .	21
1.5 $v_2$ versus $p_T$ and $KE_T$ for various collision systems. . . . .	22
1.6 $v_2$ versus $p_T$ and $KE_T$ for various collision systems scaled by the number of valence quarks. . . . .	23
1.7 $R_{AA}$ versus $p_T$ for direct $\gamma$ , $\pi^0$ , and $\eta$ . . . . .	24
1.8 STAR measured h-h correlations . . . . .	25
1.9 Leading order direct $\gamma$ production mechanisms . . . . .	26
1.10 Photon $v_2$ versus $p_T$ with systematic errors . . . . .	28
1.11 $\pi^0 v_2$ versus $p_T$ with systematic errors . . . . .	29
2.1 An aerial view of RHIC. . . . .	31
2.2 PHENIX configuration for 2010. . . . .	33
2.3 BBC single element and a module. . . . .	35
2.4 ZDC position in relation to the beamline. . . . .	36
2.5 Centrality. BBC charge versus ZDC energy. . . . .	37
2.6 A module of PbSc and PbGl, both used in EMCal. . . . .	39
3.1 Acceptance correction process . . . . .	44
3.2 Accepted trigger and reaction plane angles . . . . .	45
3.3 Acceptance corrected associated-reaction plane correlation. . . . .	46
3.4 Trigger-associated pair acceptance function and corrected trigger-associated correlation. . . . .	50
3.5 Visualization of the isolation cut . . . . .	52
3.6 Accepted triggers when isolation cut is applied . . . . .	53
3.7 Trigger-associated particle correlation when the isolation cut is applied. . . . .	53
3.8 $N_{\text{Poisson}}$ distributions for cones in and out of reaction plane. . . . .	54
3.9 Cone efficiency as a function of $\Delta\phi$ . . . . .	55
3.10 Trigger-reaction plane correlation for sophisticated MC simulation. . . . .	55
4.1 Invariant mass of photon pairs, used for $\pi^0$ selection . . . . .	58
4.2 Example $\Delta\phi$ distribution used to extract $v_2$ . . . . .	61
4.3 Resolution correction for the BBC . . . . .	62
4.4 Isolated photon $v_{2\text{effective}}$ versus $p_T$ for 0-20% centrality . . . . .	63
4.5 Isolated photon $v_{2\text{effective}}$ versus $p_T$ for 20-40% centrality . . . . .	63
4.6 Isolated photon $v_{2\text{effective}}$ versus $p_T$ for 40-60% centrality . . . . .	64
4.7 Isolated photon $v_{2\text{effective}}$ versus $p_T$ for 60-92% centrality . . . . .	64

4.8 Isolated $\pi^0 v_{2\text{effective}}$ versus $p_T$ for 0-20% centrality . . . . .	65
4.9 Isolated $\pi^0 v_{2\text{effective}}$ versus $p_T$ for 20-40% centrality . . . . .	65
4.10 Isolated $\pi^0 v_{2\text{effective}}$ versus $p_T$ for 40-60% centrality . . . . .	66
4.11 Isolated $\pi^0 v_{2\text{effective}}$ versus $p_T$ for 60-92% centrality . . . . .	66
4.12 Inclusive photon $v_{2\text{effective}}$ versus $p_T$ for 0-20% centrality . . . . .	68
4.13 Inclusive $\pi^0 v_{2\text{effective}}$ versus $p_T$ for 0-20% centrality . . . . .	68
4.14 Resolution corrected $v_2$ versus $p_T$ for isolated photons with 0-20% centrality for eight event planes . . . . .	69
4.15 Ratio of isolated photon $v_2$ to inclusive photon $v_2$ versus $p_T$ for 0-20% centrality for eight event planes . . . . .	70
5.1 $E_{\text{cone}}$ distributions for cones in and out of the event plane. . . . .	73
5.2 Cone efficiency as a function of $\Delta\phi$ . . . . .	73
5.3 $v_3$ versus $p_T$ for 20-40% centrality inclusive photons . . . . .	75
5.4 $v_3$ versus $p_T$ for 20-40% centrality $\pi^0$ . . . . .	75

# 1 INTRODUCTION

## 1.1 The Standard Model

The standard model of particle physics is a theory that encompasses subatomic particles and the forces that act on them. Particles are divided into three classes, gauge bosons, quarks, and leptons. There are four fundamental forces in nature: gravity, strong, weak, and electromagnetic. The latter three are included in the standard model.

### 1.1.1 Gauge Bosons

The strong and weak force act on extremely short distances (less than 1 fm) while the electromagnetic and gravity are infinite in range. The strong force forms hadrons by holding quarks together through the exchange of gluons and is described by Quantum Chromodynamics (QCD). The weak force is responsible for radioactive decay and fusion, is mediated by W and Z bosons, and can be described using Quantum Flavordynamics (QFD). Photons carry the electromagnetic force between charged particles. The electromagnetic force is described by quantum electrodynamics (QED). The electro-weak theory merges QFD and QED above an energy of 100 GeV. Gravity is theorized to be mediated by the graviton, a massless boson yet to be observed. A summary of the fundamental forces and gauge bosons can be seen in Table 1.1.

Table 1.1: The fundamental forces with their theories and mediators. The only mediators with mass are the mediators for the weak force. All mediators are bosons and have integer spin. The ranges of the strong and weak forces are very small while the ranges of the electromagnetic and gravitational forces have infinite range [1].

Interaction	Theory	Mediator	Mass (GeV/c <sup>2</sup> )	Range (m)
Strong	Quantum Chromodynamics	gluon	0	10 <sup>-15</sup>
Weak	Quantum Flavordynamics	W <sup>±</sup> , Z <sup>0</sup>	80.4, 91.2	10 <sup>-18</sup>
Electromagnetic	Quantum Elecrodynamics	photon	0	$\infty$
Gravity	General Relativity	graviton	0	$\infty$

These is another notable boson that should be mentioned, the Higgs boson. It was predicted by the standard model after the prediction of the Higgs mechanism and Discovered in July 2012. It has no charge, spin or color and is very unstable. It creates a Higgs field that causes particles to acquire mass. The Higgs mechanism causes the W and Z have mass because they couple to the Higgs field.

### 1.1.2 Quarks

There are six types of quarks: up, down, charm, strange, top, and bottom. The theory of QCD requires three color charges, resulting in 18 types of quarks (see section 1.1.4). Quarks can be combined two ways: three quark systems, called baryons (i.e. proton, neutron,  $\Lambda$ ) or quark antiquark systems, called mesons (i.e.  $\pi^+$ ,  $\pi^0$ ,  $K^-$ ). Baryons and mesons are collectively named hadrons because they are composed of quarks. The charge of an individual quark is less than the charge of an election,  $e^-$ , and is always divisible by

three because they combine to form integer charges. A quark summary can be seen in Table 1.2.

Table 1.2: The quarks with their masses and charges. All quarks are fermions requiring their spin to be one half [1].

Quark	Charge ( $e$ )	Mass (MeV/c $^2$ )
up	+2/3	1.7 - 3.1
down	-1/3	4.1 - 5.7
charm	+2/3	1290
strange	-1/3	100
top	+2/3	4190
bottom	-1/3	172900

### 1.1.3 Leptons

The last main class of particles is leptons. There are six leptons: electron, muon, tau, electron neutrino, muon neutrino, and tau neutrino. The electron, muon, and tau have charge  $-e$  while all neutrinos are neutral. Taus are the most massive leptons, followed by muons, and then electrons, while neutrinos are the least massive. All neutrinos have a small nonzero mass; because of this, the mass hierarchy is difficult to determine. See Table 1.3 for a summary of leptons.

Table 1.3: The leptons with their masses, charges and lifetimes.

Tau is the most massive and fastest decaying lepton. The neutrino masses are approximately zero. All leptons have half integer spin [1].

Lepton	Charge ( $e$ )	Mass (MeV/c $^2$ )	Lifetime (s)
electron	-1	0.511	$\infty$
electron neutrino	0	$\approx 0$	$\infty$
muon	-1	105.7	$2.2 \times 10^{-6}$
muon neutrino	0	$\approx 0$	$\infty$
tau	-1	1777	$2.91 \times 10^{-13}$
tau neutrino	0	$\approx 0$	$\infty$

Each quark and lepton have a corresponding antiparticle with the opposite quantum numbers, such as charge and spin. Antiquarks can combine with quarks to form a myriad of types of mesons and baryons. The fundamental forces act in the same manner for both particles and antiparticles.

#### 1.1.4 Quantum Chromodynamics

Quantum chromodynamics (QCD) is the theory of the strong force that works through the exchange of color-charged-mediators called gluons. The color charges are defined to be red, green, or blue. There are also anti charges, anti-red, anti-green, and anti-blue. Quarks and gluons do not actually have color; the use of color is to signify three different charges. All hadrons are colorless. Mesons contain a colored quark and an anti-colored antiquark, the color must be the same so that the meson is color neutral. In Baryons, the three colors may combine to become neutral. For example, the  $\Delta$  baryon, a

$uuu$  system, contains one quark of each color in order for it to be colorless. This must be true in order for quarks to be fermions, because they are required to obey the Pauli exclusion principle.

The strong force causes the quarks to be confined in the hadrons, a phenomena called quark confinement. If the distance separating the quarks gets larger, the force gets stronger. If enough energy and density is given to the quarks they can overcome the strong force and form a new state of matter called a quark gluon plasma (QGP). Figure 1.1 shows the QCD phase diagram, temperature versus net baryon density (i.e. density of protons, neutrons) with the phase transition labeled. Normal matter is in the lower left, hadron gas phase. Notice that the current RHIC experiments have a low baryon density and high temperature.

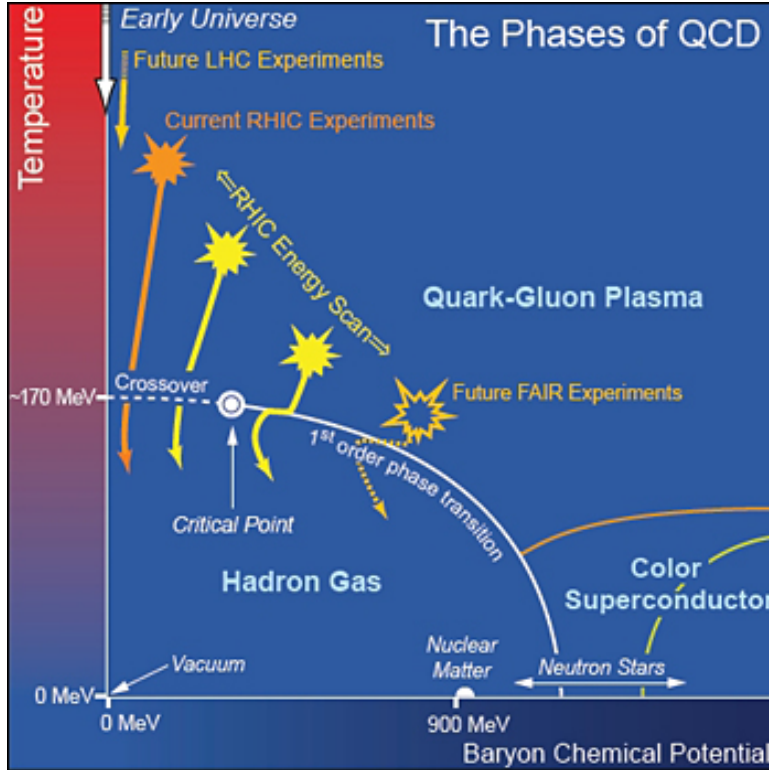


Figure 1.1: QCD phase diagram showing the phase transition from hadron gas to quark gluon plasma [2].

The Universe existed in a quark gluon plasma phase for a few millionths of a second immediately after the big bang [3]. It was in this phase due to an extremely high energy density causing a high temperature. At one second, it had expanded and cooled enough for a phase transition to occur and hadrons to form. Understanding how QGP interacts will help determine how the universe behaved right after the big bang and why it is the way it is today. More importantly, understanding how the QGP behaves provides for probes of the non-perturbative region of QCD. This region is hard to probe theoretically because calculations must be done using a computationally intensive technique called lattice QCD.

## 1.2 Heavy Ion Collisions

It is impossible to squeeze baryons to increase their density so that they undergo the phase transition to a QGP on Earth. As seen in Figure 1.1, this can happen inside neutron stars. On Earth, the only way to form a QGP is to increase the baryons temperature by colliding it with another baryon at nearly the speed of light. Only two facilities can do this, the Large Hadron Collider (LHC) in Geneva, Switzerland [3] and the Relativistic Heavy Ion Collider (RHIC) in Upton, New York [4].

### 1.2.1 Event Evolution

The Relativistic Heavy Ion Collider forms QGP by colliding gold ions at 99.999% the speed of light ( $c$ ). At that velocity the energy per nucleon pair of the reaction center of mass frame ( $\sqrt{s_{NN}}$ ) is 200 GeV. A typical gold nucleus has a diameter of about 15 fm, but when accelerated to 99.999% $c$ , it is Lorentz contracted along the direction of travel to a 0.13 fm thick disk. This contraction causes the ions to only overlap during the collision for  $4.38 \times 10^{-25}$  s (0.13 fm/c). Not all collisions have complete overlap of the nuclei. A large overlap produces a large number of participants, while small overlap has a large number of spectators. Particles that interact in the collision are called participants and particles that fly by the collision are named spectators. Outgoing particles with high transverse to the beamline momentum ( $>5$  GeV/c) are called jets. They get their momentum from hard scattering processes of the parent nuclei's quarks or gluons. After the collision, the QGP expands and cools which causes it to transition back to hadrons. This phase transition is called hadronization. At this point in the event, the quark flavors inside the hadrons are fluctuating due to inelastic scattering of the hadrons. After further expansion and cooling, chemical freeze out occurs, ceasing inelastic scattering; this causes the flavors of the quarks to stop changing. Thermal freeze out occurs after more expansion when the outgoing hadrons and leptons are no longer interacting. Now, they can decay if it

is energetically favorable. Once all of this occurs, the outgoing particle's momenta and type are identified by detectors. This entire process is called an event. Figure 1.2 shows a simulation of a single event.

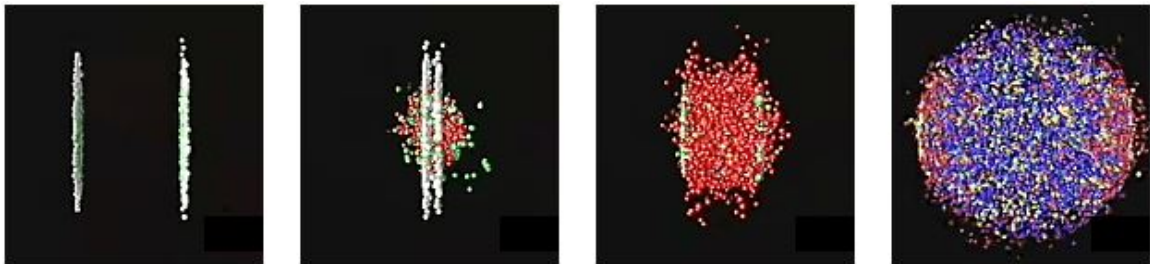


Figure 1.2: Time flows from left to right. The leftmost panel shows the Lorentz contracted gold nuclei. In the middle left panel the ions collide. The red spheres in the next panel are the deconfined quarks and gluons. The rightmost panel shows the expanding quark gluon plasma [4].

## 1.2.2 Event Characterization

### 1.2.2.1 Centrality

Since each event is unique, there is a set of variables used to classify them. The most descriptive of these is the distance separating the center of the colliding nuclei, or impact parameter,  $b$ . For small  $b$ , the overlap between the nuclei is large and the number of participants is large. For large  $b$ , the overlap is small and there are a small number of participants. Unfortunately, impact parameters cannot be measured directly. Instead, a variable called centrality is used. The centrality of the current collision is the percentage of collisions with larger multiplicity than the current collision. Multiplicity is the number of particles created in the collision. Events with large multiplicity are named central, while small multiplicity events are called peripheral (see Figure 1.3).

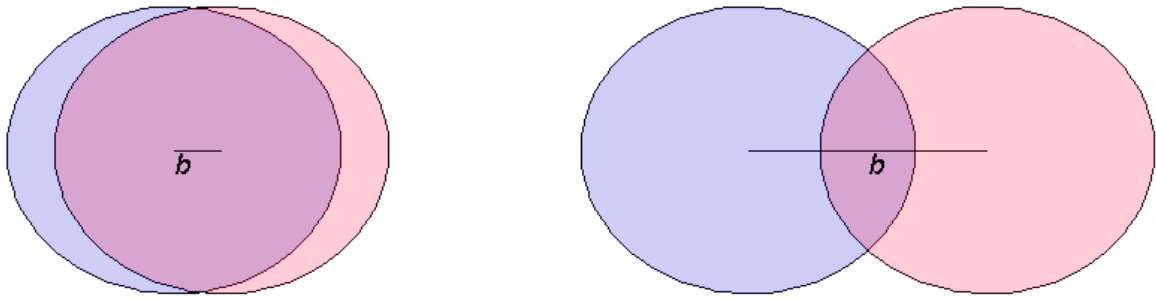


Figure 1.3: Centrality examples with the impact parameter labeled: (Left) Central collisions, (Right) Peripheral collisions. The beamline is out of the page.

### 1.2.2.2 Coordinate Systems

A few coordinate systems can be placed about the nominal collision point in order to map out where the outgoing particles travel. A Cartesian coordinate system with the  $+z$  axis along one of the beam lines and the  $+y$  axis straight up is the most convenient. A spherical system can also be used with  $\theta$  defined as the angle above the beam line with  $\theta = 0$  along the  $+z$  axis and  $\phi$  defined as the angle around the beam line, with  $\phi = 0$  along the  $+x$  axis.

There are two useful unit less variables, rapidity( $y$ ) and pseudorapidity ( $\eta$ ), that describe forward and backward angles with respect to the nominal collision point and beamline. Rapidity is defined as

$$y = \frac{1}{2} \ln \frac{1 + \beta \cos \theta}{1 - \beta \cos \theta} = \frac{1}{2} \ln \frac{1 + \beta_z}{1 - \beta_z} \quad (1.1)$$

where  $\beta = v/c$  and  $v$  is the particles velocity. It conveys a particle's velocity along the beam line, its velocity in the  $+z$  direction,  $\beta_z = v_z/c$ . The problem with rapidity is that it requires knowing the particles velocity. The better quantity, pseudorapidity, only relies on the particles angle. It is defined as

$$\eta = \frac{1}{2} \ln \frac{1 + \cos \theta}{1 - \cos \theta}. \quad (1.2)$$

Notice that as a particles velocity approaches the speed of light,  $\beta$  goes to one and rapidity and pseudorapidity are equal except at  $0^\circ$  and  $180^\circ$ .

### 1.2.2.3 Reaction Planes

The plane defined by the impact parameter and the beamline is called the reaction plane. The angle of this plane ( $\Psi_{RP}$ ) with respect to the beamline is measured by determining the azimuthal asymmetry of the outgoing particles. The asymmetry is described by [5]

$$\frac{d(N)}{d(\phi - \Psi_{RP})} = \frac{\langle wN \rangle}{2\pi} \left( 1 + 2 \sum_{n=1}^{\infty} v_n \cos \left( km (\phi - \Psi_{RP_n}) \right) \right), \quad (1.3)$$

a Fourier expansion where  $N$  is the number of detected particles,  $w$  a weight associated with those particles,  $n$  is the harmonic of the produced particle distribution,  $m$  is the harmonic of the reaction plane angle that is further explained below,  $k$  is a multiplicative factor so  $n = km$ ,  $\phi$  is the azimuthal angle of the outgoing particle, and the Fourier coefficient,

$$v_n = \langle \cos ( km (\phi - \Psi_{RP}) ) \rangle, \quad (1.4)$$

is called the flow coefficient. The angle brackets indicate an average over particles in all events. The flow coefficient is the magnitude of the azimuthal anisotropy. Any  $v_n$  can be measured with any reaction plane harmonic  $m$  as long as  $n \geq m$  and  $n$  is a multiple of  $m$ . This means that all  $v_n$  can be measured with  $m = 1$ , but only even  $v_n$  can be measured with  $m = 2$ . The coefficient  $v_1$  is often called direct flow,  $v_2$  is called elliptic flow, and  $v_3$  is called triangular flow. Equation 1.4 describing particle flow, has been verified using both hydrodynamic models and heavy ion collisions.

The reaction plane angle cannot be known with full certainty because there are fluctuations in the partons that participate in the collision. If each nucleus is considered a collection of billiard balls, when they collide, one cannot know with full certainty the plane in which the collision took place. This uncertainty causes a new variable to be used instead of the reaction plane, it is called the event plane angle ( $\Psi_{EP}$ ) and is used to signify the reaction plane without full certainty. Each harmonic of the particle's azimuthal distribution has its own event plane, and is described by

$$\begin{aligned}\Psi_n &= \frac{1}{n} \arctan \frac{Y_n}{X_n}, \\ Y_n &= \sum_{i=1}^N w_i \sin(n\phi_i) \\ X_n &= \sum_{i=1}^N w_i \cos(n\phi_i)\end{aligned}\tag{1.5}$$

where the sum over  $i$  is a sum over particles in the collision,  $w_i$  is a weight associated with the particle, and  $\phi_i$  is the azimuthal angle of that particle. The flow vectors  $X_n$  and  $Y_n$  are along the  $x$  and  $y$  axis, respectively.

Elliptic flow originates from the initial collision geometry. As seen in Figure 1.3a, in a high  $v_2$  collision, the participants form an ellipsoid that must thermalize. The thermalization process forms a pressure gradient that is strongest on the shortest axis of the ellipse, along the event plane, as indicated by the long blue arrows. This pressure gradient makes the QGP expand nonuniformly and generate the particle asymmetry as described by Equation 1.3.

The higher order flow harmonics are present in all collisions because the colliding nuclei are not perfect liquid drops. They can be considered as a collection of discrete spherical partons. This makes the participants less of an almond shape.  $\Psi_2$  is closest to the true reaction plane. As seen in Figure 1.3b,  $\Psi_3$  encompasses more participants than  $\Psi_2$ , and  $\Psi_4$  contains all of the participants. One can see that if the azimuthal asymmetry, Equation 1.3, were to be truncated at  $n = 2$ , it would approximately describe this collision but it would be more accurate to include the higher order terms.

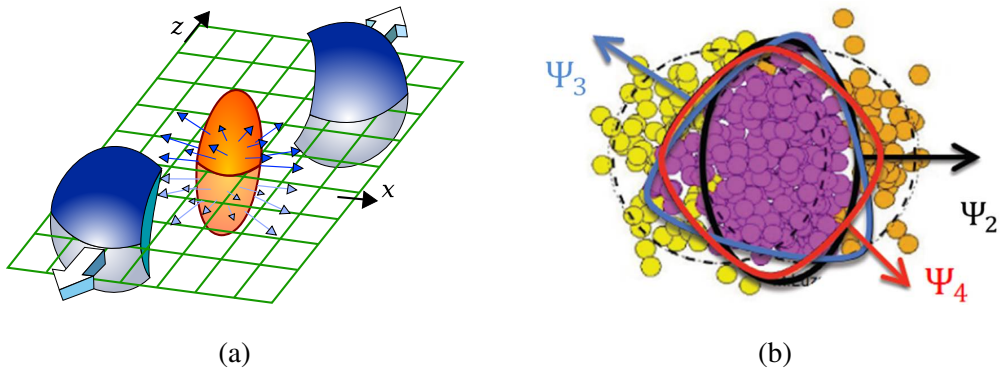


Figure 1.4: (a) A typical collision with purely elliptic flow. The participants form the almond shape (orange ellipsoid) while the spectators continue to travel along the beamline (blue spheres). The green grid is the reaction plane. The blue arrows show the direction of the pressure that's largest in the plane and smallest outside the plane. (b) A typical collision cross section with the higher order harmonic reaction planes labeled. The beamline is out of the page. The participants are the purple spheres while the spectators are the orange and yellow spheres. The reaction planes,  $\Psi_2$ ,  $\Psi_3$ , and  $\Psi_4$ , are labeled.

One can see from Equation 1.5, that each  $\Psi_n$  has different maximum and minimum values according to it's harmonic. Explicitly, this means

$$\begin{aligned} -\frac{\pi}{2} &\geq \Psi_2 \geq \frac{\pi}{2}, \\ -\frac{\pi}{3} &\geq \Psi_3 \geq \frac{\pi}{3}, \text{ and} \\ -\frac{\pi}{4} &\geq \Psi_4 \geq \frac{\pi}{4}. \end{aligned} \tag{1.6}$$

### 1.2.3 QGP Signatures

Signatures that show that a heavy ion collision formed a QGP are harmonic flow, single particle suppression, and jet suppression. All three of these factors are large fields of study in heavy ion physics. Typically, measured quantities in heavy ion collisions are

compared to the same quantities in p+p collisions. This is because a QGP is not expected to form in p+p collisions.

### 1.2.3.1 Harmonic Flow

The second order flow coefficient,  $v_2$  has been measured by two experiments at RHIC: PHENIX and STAR. These coefficients are often plotted versus transverse momentum ( $p_T$ ) or transverse kinetic energy ( $KE_T$ ). Figure 1.5 shows  $v_2$  versus  $p_T$  and  $KE_T$  for different collision systems. One can see that at high  $p_T$  and  $KE_T$  the systems fall into two groups, the baryon collision systems and the meson collision systems. If the  $v_2$  values are scaled by the number of valence quarks ( $n_q$ ), there is no longer any separation (see Figure 1.6). This is evidence that it is not the hadrons that cause the anisotropy, but the quarks.

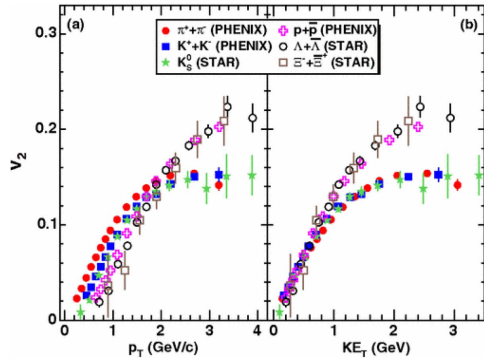


Figure 1.5: Elliptic flow coefficient  $v_2$  versus  $p_T$  and  $KE_T$  for various collision systems. The meson and baryon collision systems separate at high  $p_T$  [6].

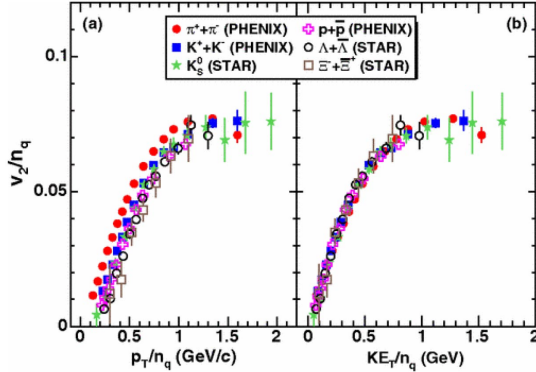


Figure 1.6: Elliptic flow coefficient  $v_2$  versus  $p_T$  and  $KE_T$  for various collision systems scaled by the number of valence quarks. The mesons and baryon collision systems are no longer separate at high  $p_T$ , proving the quarks are causing the anisotropy, not the hadrons [6].

### 1.2.3.2 Single Particle Suppression

Naively, one expects the number of particles produced in heavy ion collisions to be a multiplicative factor times the number of particles produced in p+p collisions. This is because heavy ion collisions are just a collection of p+p collisions happening at one time. This expectation turns out to be false because the QGP in heavy ion collisions suppresses the particle production. This can be seen in Figure 1.7 which shows the nuclear modification factor,  $R_{AA}$ , versus  $p_T$  for direct photon and two different mesons. For Au+Au collisions,

$$R_{AA} = \frac{1}{N_{coll}} \frac{d^2N^{AA}/dydp_T}{\langle T_{AA} \rangle d^2\sigma_{pp}/dydp_T}, \quad (1.7)$$

where  $N_{coll}$  is the effective number nucleon nucleon collisions for an equivalent p+p collision,  $d^2N^{AA}/dydp_T$  is the invariant yield of the Au+Au collision,  $d^2\sigma_{pp}/dydp_T$  is the p+p cross section, and  $\langle T_{AA} \rangle$  is a scale factor, called the nuclear thickness function, that is determined using a Glauber Monte Carlo calculation.

The direct photons are not suppressed because they are not affected by the QGP while the mesons show a suppression factor of about 5.

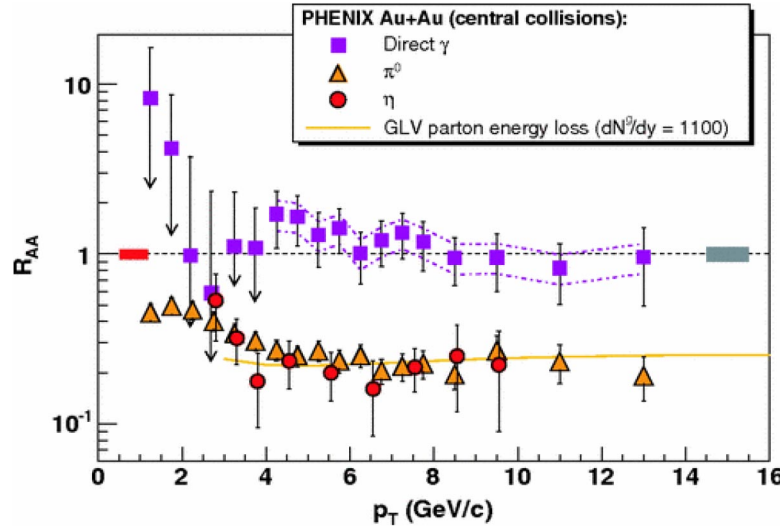


Figure 1.7: Suppression factor  $R_{AA}$  versus  $p_T$  for direct photons,  $\pi^0$ , and  $\eta$ . The  $\pi^0$ , and  $\eta$  show suppression, while direct photons do not [7].

### 1.2.3.3 Jet Suppression

Determining what particles composed a jet is a nontrivial task. There are two general methods which determine if a particle makes up a jet, a direct method and an indirect method. The direct method consists of a jet reconstruction algorithm that tags individual particles then determines whether or not they are in a jet according to the predefined algorithm. This method is highly effective in p+p collisions but it has difficulties in heavy ion collisions because there are a copious amount of underlying high  $p_T$  particles that increase the algorithm's probability of tagging false jets.

A alternative technique for heavy ion collisions is the indirect method. In this method, the two particle correlation is measured. Two particle correlations consist of the correlation between two particles as a function of their azimuthal difference, as seen in

Figure 1.8. The peak at  $\Delta\phi = 0$  is called the near-side peak; it is caused by particles that have no azimuthal angle difference therefore they are particles from the same jet. The peak at  $\Delta\phi = \pi$  is called the away-side peak; it is caused by particles that have maximum azimuthal angle difference. They are particles from opposite jets. These jets originate from the hard scattering processes that take place at the beginning of the collision. Figure 1.8 shows high  $p_T$  charged hadron-hadron (h-h) correlations measured by STAR for three different collision systems. The Au+Au collisions have no away-side peak. This indicates that the jet that has to travel through the QGP loses all of its energy before it makes it through the medium. The lack of away-side jet is called jet suppression.

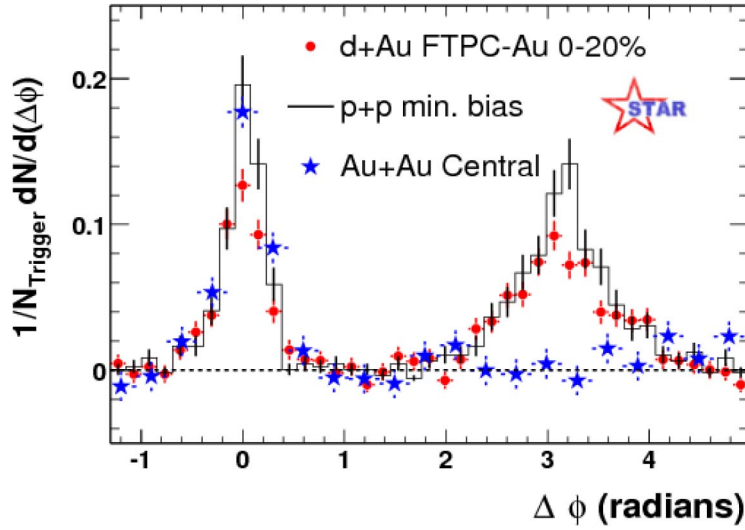


Figure 1.8: h-h correlations with a high  $p_T$  trigger measured by STAR for 3 collision systems. Only the away-side Au+Au jets are suppressed [8].

When making correlation measurements, one should be cautious of the QGP's surface bias. A surface bias occurs if only high  $p_T$  trigger particles (the first particle in the correlation) are sampled because the associated particles (the second particle) lose most, if

not all, of their energy when they travel through the medium. This process is called surface bias because very high  $p_T$  particles originate from the surface of the QGP.

Instead of measuring h-h correlations, direct photon-hadron ( $\gamma_{dir}$ -h) correlations are often preferred. There are several reasons for this, one is because there is no way to get the h-h jet momentum; it must be approximated through a jet reconstruction algorithm. Another is because of surface bias discussed in the previous paragraph. Also, since both jets may be modified by the QGP, it is hard to get their true energy. Direct photons are photons that are created through hard scattering processes such as annihilation ( $q\bar{q} \rightarrow g\gamma$ ) and Compton scattering ( $qg \rightarrow q\gamma$ ) as seen in Figure 1.9. Direct photons are colorless entities and therefore not affected by the QGP. Because of this, many of the problems with h-h correlations are solved. Conservation of momentum implies that the energy of the photon is the same as the energy of the hadron jet. Since the photons emitted are colorless and do not interact inside the QGP they suffer no surface bias.

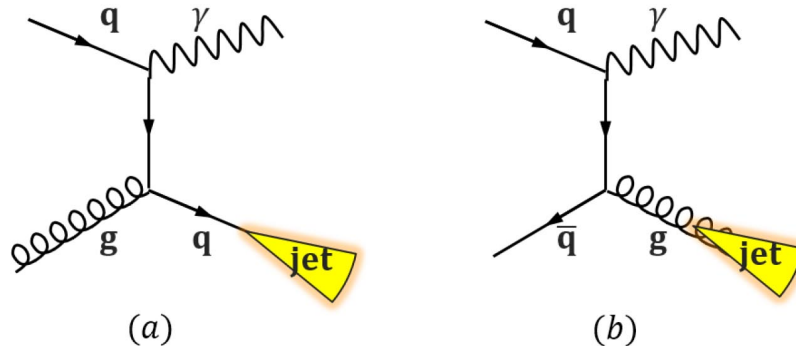


Figure 1.9: Leading order direct  $\gamma$  production mechanisms, annihilation ( $q\bar{q} \rightarrow g\gamma$ ) (Right) and Compton scattering ( $qg \rightarrow q\gamma$ ) (Left) [9].

There is a problem with using  $\gamma_{dir}$ -h correlations. Many different types of photons are created in each event and deciphering which ones are direct is difficult to do. Inclusive

photons are all the photons in the event but they can be further classified into two categories, decay and non-decay. Most decay photons are created in the decay of  $\pi^0$  mesons, others come from decays of underlying event hadrons. Direct photons are generally isolated because they are created from the initial collision and do not form jets. Determining which photons are isolated is simple. A cone is fit around the photon, the energy of the particles inside the cone is measured and if the energy is less than a certain threshold, the photon is isolated. This process is called the isolation cut method.

The underlying background pairs exhibit anisotropic flow as described by Equation 1.3. If particles with this distribution are paired with one another they would produce a similar distribution. This distribution is described by multiplying Equation 1.3 for particle  $A$  with Equation 1.3 for particle  $B$ ,

$$\frac{dN_{comb}^{AB}}{d\Delta\phi_{AB}} \propto 1 + 2v_2^A v_2^B \cos(2\Delta\phi_{AB}) + 3v_3^A v_3^B \cos(3\Delta\phi_{AB}) + \dots \quad (1.8)$$

This equation can be truncated after the  $n = 2$  term because the higher order terms can be considered perturbations to the elliptic shape. Equation 1.8 is often called the combinatoric background distribution. In order to get the jet's correlation function the background pair distribution must be subtracted from the raw correlation function.

### 1.3 Flow Coefficient Determination and Systematic Errors

Previous measurements of  $v_2$  for inclusive photons and  $\pi^0$ 's have been performed by [10]. These are shown in Figures 1.10 and 1.11. These values are used for subtracting the underlying event  $v_2$  in jet correlation studies. In the peak at low  $p_T$ , hydrodynamic flow contributions dominate. For all  $p_T$  there is a small contribution from energy loss, caused by particles flowing through different parts of the QGP. This is especially evident in the nonzero  $v_2$  at high  $p_T$ .

The systematic error on the these measurements includes errors on a few key steps in the determination of the elliptic flow coefficient. There is hadron contamination in the detection of low  $p_T$  photons. The  $v_2$  coefficient can be calculated by fitting the azimuthal distribution (Equation 1.3) or calculating the average of the cosine directly (Equation 1.4). The percent difference between the two methods was included in the systematics. There is error associated with the determination of the event plane caused by fluctuations in the measured  $v_2$  value, flattening of the reaction plane angles, the number of coefficients used in the flattening procedure, and run-by-run dependences [10]. All of these errors are included in the brown boxes behind the data points in Figure 1.10.

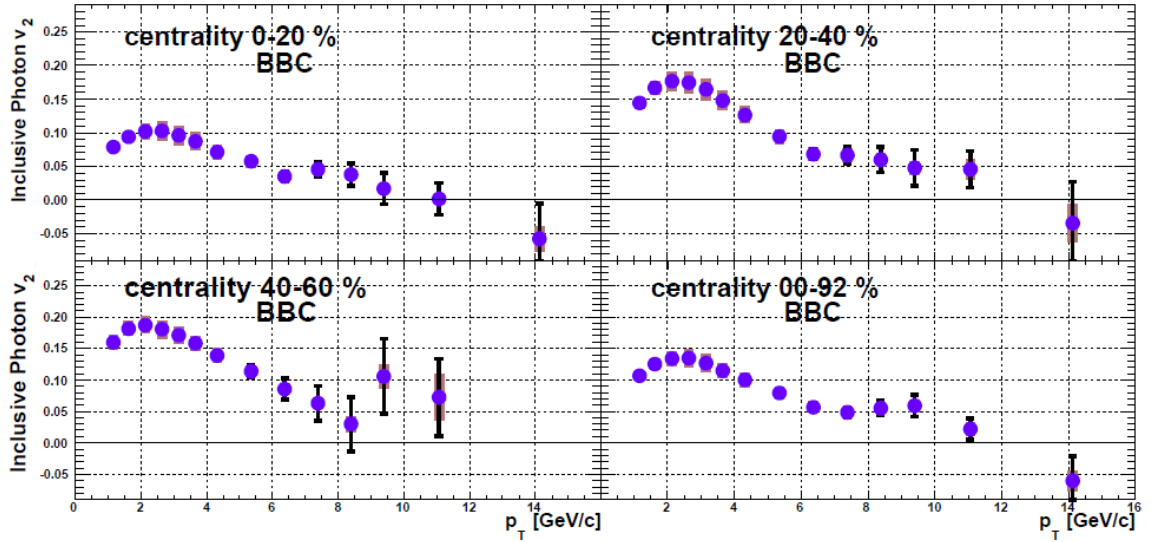


Figure 1.10: Photon  $v_2$  versus  $p_T$  with systematic errors (Brown Boxes). [10]

The sources of systematic error for the  $\pi^0$  analysis include: combinatoric photon-photon pair background subtraction, particle identification, photon-photon shower merging and reaction plane determination. The particle identification errors are determined by changing the  $\pi^0$  selection definitions and observing how it affects the measured  $v_2$ . The decay of the  $\pi^0$  causes the detector to only see one big electromagnetic

shower instead of two smaller ones. This effect is quantified by changing the threshold for the energy of the cluster to accept more merged clusters and observe how the output  $v_2$  behaves. The  $\pi^0$  have the same errors as the photons for the reaction plane determination [10]. All of these errors are included in the brown boxes behind the data points in Figure 1.11.

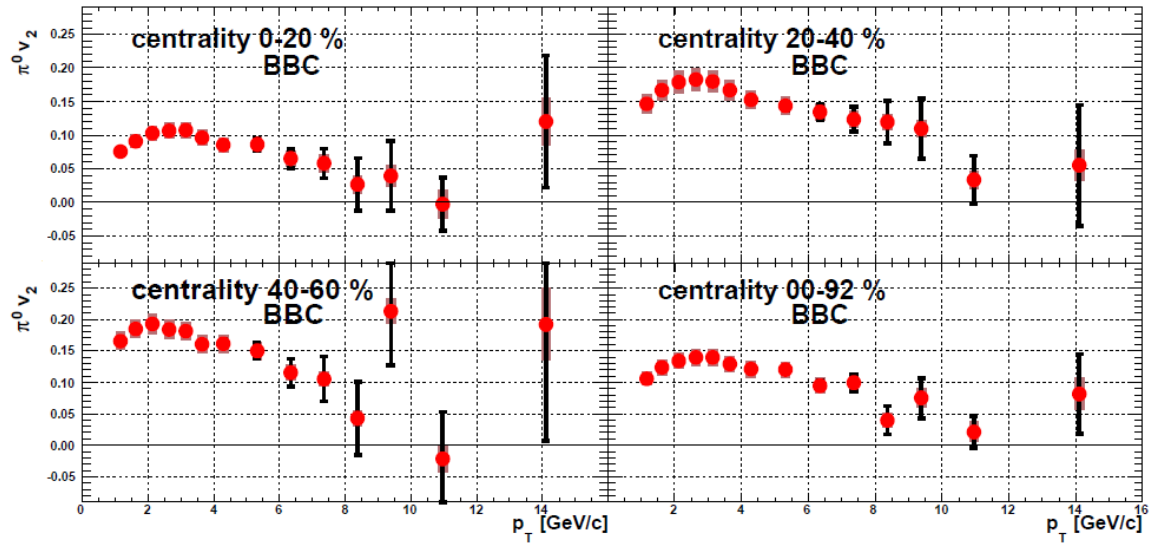


Figure 1.11:  $\pi^0 v_2$  versus  $p_T$  with systematic errors (Brown Boxes). [10]

Detailed tables explaining the systematic errors, including the size from each source separately, can be found in [10].

#### 1.4 Motivation of This Thesis

This project is dedicated to measuring the elliptic flow coefficients of isolated photons and determining the correct coefficient for the two particle correlation function (Equation 1.8). A meticulous measurement these coefficients is required in order to construct an accurate jet function. Many measurements rely on this jet function, for these it is imperative that the jet function be correct. Initial measurements of  $\gamma_{iso} v_2$  produced

unanticipated results. The values were too small and often negative. This leads us to believe there is a reaction plane dependent efficiency for the isolation cut. Factoring in this efficiency requires Equation 1.8 to be rederived and confirmed using a Monte Carlo simulation. The initial measurements are then amended to include this efficiency modification.

This thesis is laid out in an atypical fashion. The introduction was motivated by [11] and [9]. Chapter two discusses the experiment used to take the data. The analysis, discussion, and results of each major topic are discussed in their own chapter in order for it to be more clear to the reader. Chapter three examines the Monte Carlo simulations and derivation of the efficiency included two particle correlation function. Chapter four discusses the analysis process and the data set. Chapter five explains the extraction of the true  $v_2$  values, outlines future work, and provides a summary.

## 2 EXPERIMENTAL DETAILS

### 2.1 Relativistic Heavy Ion Collider

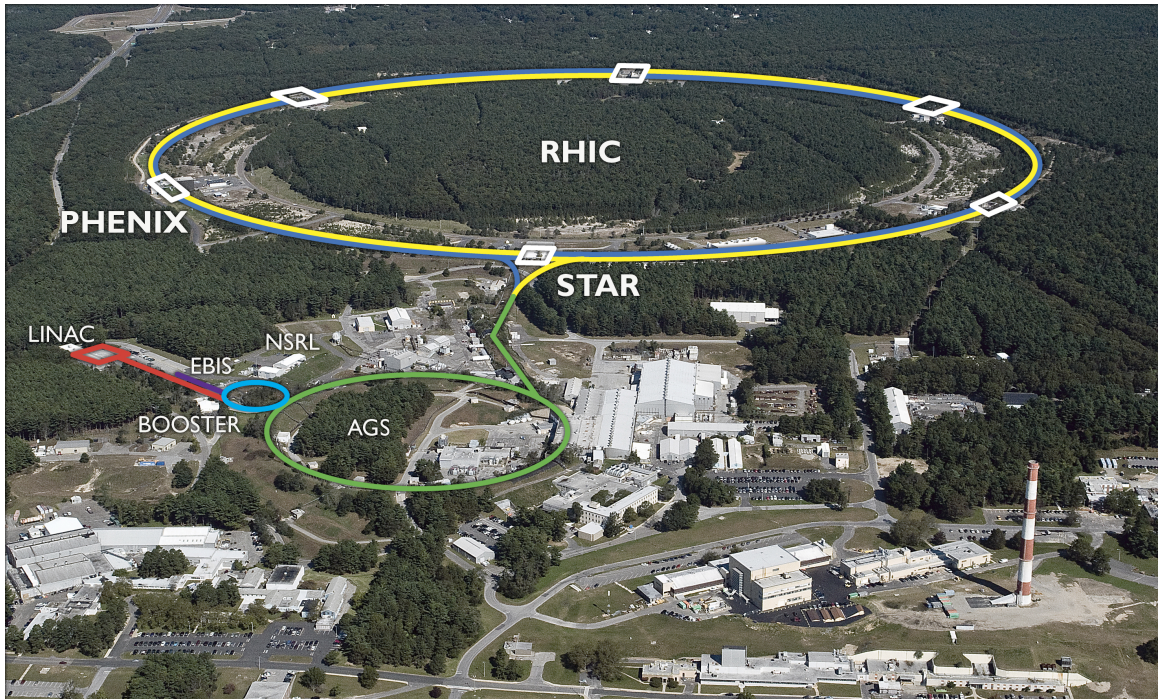


Figure 2.1: An aerial view of RHIC with the experiments and accelerators labeled.

The Relativistic Heavy Ion Collider (RHIC) is located at Brookhaven National Laboratory in Upton, New York. It consists of accelerators that bring ions from rest to 99.999 % the speed of light and two concentric 3.8 kilometer storage rings that preserve the ions until they are collided in the experimental areas. There are four experimental areas at RHIC: BRAHMS, PHOBOS, STAR and PHENIX. Only the latter two areas are still in operation. The experiment used to collect the data set used in this thesis, PHENIX, is described in the next section. RHIC is capable of colliding a myriad of types of particles at center of mass pair energies below 500 GeV.

## 2.2 Pioneering High Energy Nuclear Interaction Experiment

The Pioneering High Energy Nuclear Interaction eXperiment (PHENIX) is an array of detectors used to identify particles and their momentum emitted from the collision of ions. The experiment is overseen by a collaboration of about 500 physicists from around the world. PHENIX had its first data taking Run (Run 1) in 2000. A summary of the data taken with the array since then can be seen in Table 2.2 at the end of this chapter.

PHENIX (shown in Figure 2.2) does not have full azimuthal coverage. This is because of the large magnets that are above and below the two central arms. The azimuthal acceptance, in radians, is

$$\begin{aligned} -0.57 \geq \phi \geq 0.97, \\ 2.14 \geq \phi \geq 3.72, \end{aligned} \tag{2.1}$$

A full list of the detectors with their location and purpose is located in Table 2.1. The detectors vital to the analysis in this thesis are described in the following sections.

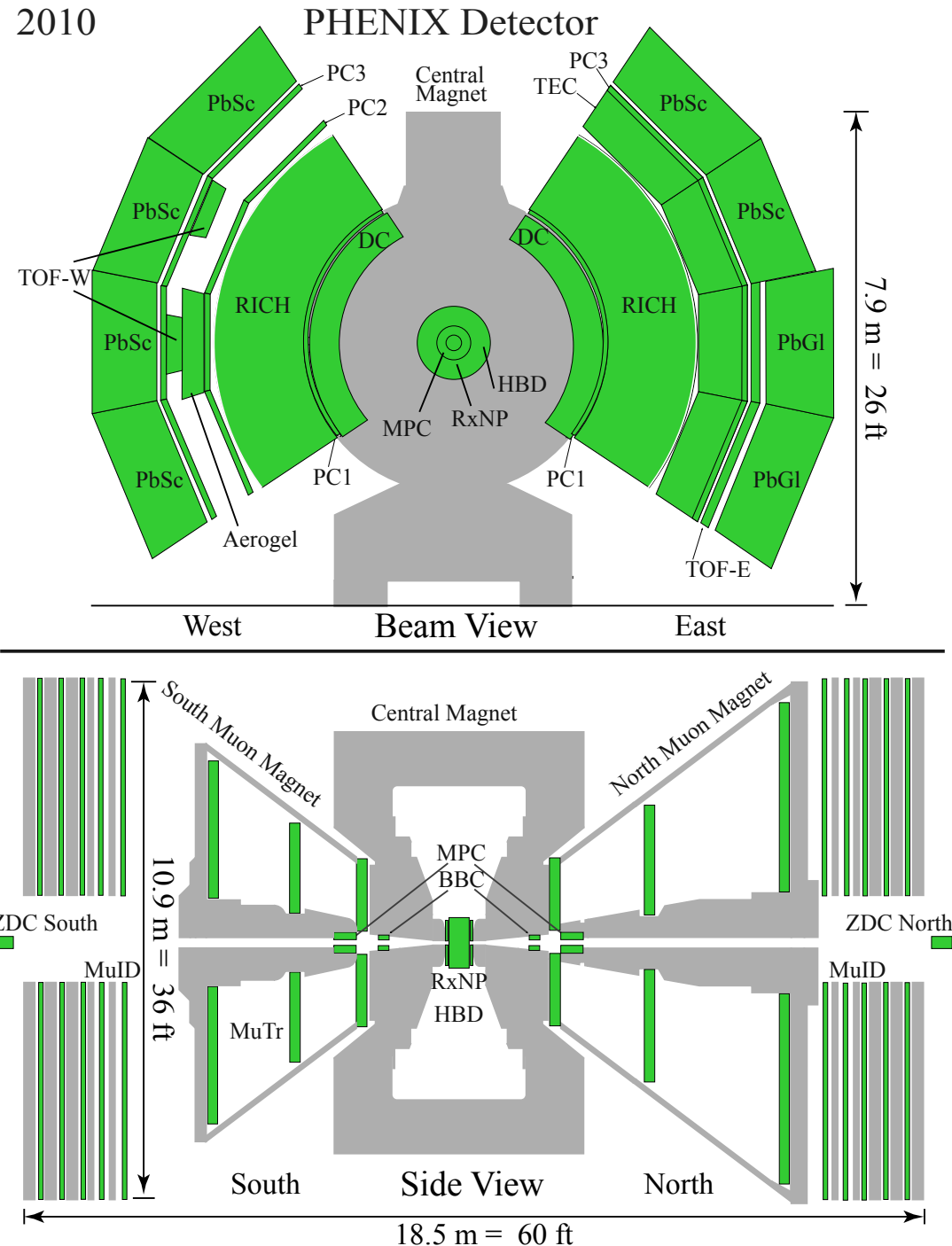


Figure 2.2: Configuration of PHENIX for Run 10 as seen along (Top) and perpendicular to the beamline (Bottom).

Detector Subsystem	$\phi$	$\eta$	Purpose
Central Magnet	$2\pi$	$ \eta  < 0.35$	Bends charged particles so they can be identified and their momentum measured
BBC	$2\pi$	$3.0 <  \eta  < 9$	Initiates timing, determines collision vertex, centrality
ZDC	$2\pi$	$\pm 2$ mrad	Determines collision vertex, centrality
RxNP	$2\pi$	$1.0 <  \eta  < 2.8$	Determines reaction plane
MPC			Measures energy in the forward
North	$2\pi$	$-3.7 <  \eta  < -3.1$	direction
South	$2\pi$	$3.1 <  \eta  < 3.9$	
EMCal			
PbSc	$\frac{\pi}{2} + \frac{\pi}{4}$	$ \eta  < 0.35$	High timing resolution, Photon identification through showers
PbGl	$\frac{\pi}{4}$	$ \eta  < 0.35$	High energy resolution and granularity
RICH	$\frac{\pi}{2} \times 2$	$ \eta  < 0.35$	Identifies electrons
DC	$\frac{\pi}{2} \times 2$	$ \eta  < 0.35$	Measures charged particles position and momentum

Table 2.1: PHENIX detectors with their acceptance and purpose. Adapted from [12]

### 2.2.1 Beam Beam Counter

The Beam Beam Counter (BBC) is made up of north and south modules, each module has full azimuthal coverage around the beam pipe and pseudorapidity  $3 < |\eta| < 3.9$ . Each module consists of 64 three centimeter long quartz Cherenkov radiators attached to photomultiplier tubes (PMTs). The detector serves five basic purposes:

- determines the collision vertex by

$$z_{vertex} = \frac{(T_S - T_N) c}{2}, \quad (2.2)$$

where  $T_S$  and  $T_N$  are the times at which the north and south modules detected hits, and  $c$  is the speed of light,

- sets time zero for the time of flight measurements,

- determines the event plane angle, and,

in conjunction with the Zero Degree Calorimeter (ZDC)

- serves as the minimum bias trigger, and

- determines collision centrality.

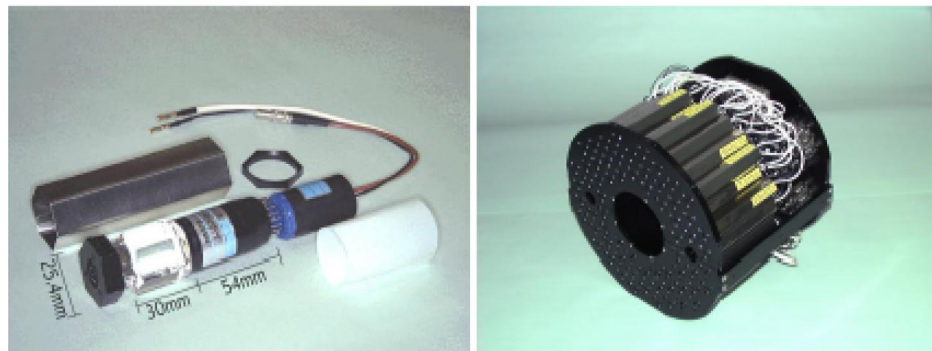


Figure 2.3: (Left) A single radiator attached to a PMT. (Right) A BBC module consisting of 64 radiators attached to PMTs [13].

### 2.2.2 Zero Degree Calorimeter

The Zero Degree Calorimeter (ZDC) consists of two modules that lie in extreme forward and backward angles, each module has full azimuthal coverage and pseudorapidity  $|\eta| > 6.0$ . They are positioned 18 m from the nominal collision vertex. They do not lie along the beamline, because that far from the vertex, the beamline curve does not align with the intersection point (see Figure 2.4). The ZDC only detects neutrons because there is a dipole magnet to deflect charged particles between it and the collision point. Each module consists of tungsten layered with fiber optics that are connected to PMTs. The reason neutron detection so far away from the collision vertex is desired is because the energy of the spectator neutrons can be used to calculate the number of participants.

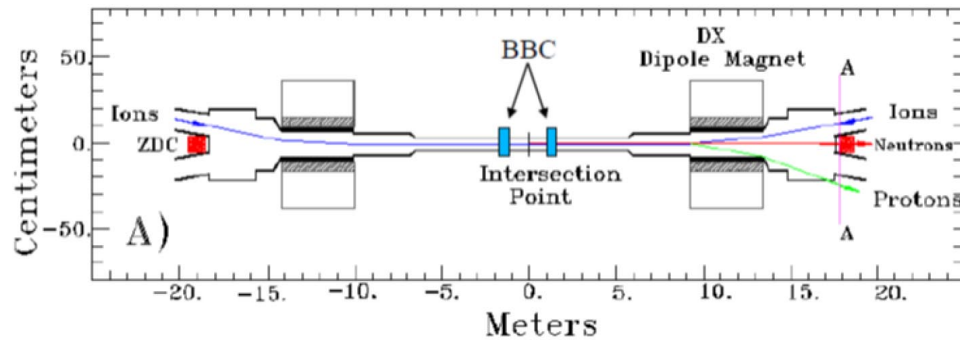


Figure 2.4: ZDC position in relation to the intersection point, BBC, and beam line [14].

To determine the collision centrality the total charge in the BBC is plotted versus the energy detected in the ZDC (see Figure 2.5). These two variables are correlated because for a central collision the number of participants is large, causing a large charge in the BBC and small neutron energy in the ZDC. The converse is also true, for peripheral collisions, the number of spectators is large and the energy deposited in the ZDC is large

while the charge detected in the BBC is small. Centrality classes are then determined by dividing this distribution such that each class contains the same number of events as shown by the labeled regions on Figure 2.5.

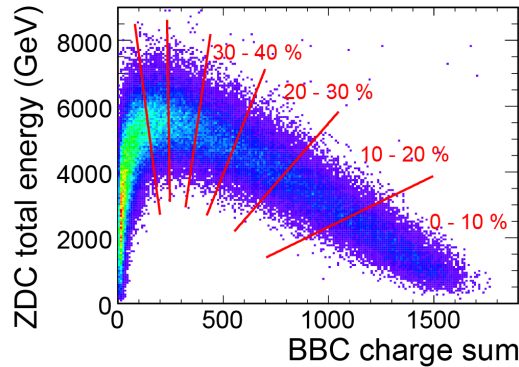


Figure 2.5: BBC charge versus ZDC energy. Centrality classes are shown in marked regions. The most central events, 0% centrality, is the region on the right. The most peripheral events are the dense region near the origin [15].

### 2.2.3 Reaction Plane Detector

The reaction plane detector (RxNP) was installed before Run 7, it consists of a north and south modules that lie outside the beam interaction area,  $38 < |z| < 40$  centimeters. Each module is made of 24 plastic scintillators attached to PMTs. The scintillators are arranged in concentric rings with full azimuthal coverage with  $1.0 < |\eta| < 1.5$  for the inner ring and  $1.5 < |\eta| < 2.8$  for the outer ring. The purpose of the RxNP is to accurately determine the event plane. Before its installation, the BBC was used to determine the event plane with the highest resolution. For the  $\Psi_2$  event plane, the resolution of the RxNP is about a factor of 2 higher than the BBC.

### 2.2.4 Muon Piston Calorimeter

The Muon Piston Calorimeter (MPC) detects photons and  $\pi^0$  both forward and backward of the collision vertex. It gets its name from its location in PHENIX, the two modules lie at the vertex ends of the muon magnets. The two modules are azimuthally symmetric but are not symmetric in pseudorapidity because of a difference of diameter of the beam pipe. The North module has a range of  $-3.7 < |\eta| < -3.1$  with 288 towers, while the South module has  $3.1 < |\eta| < 3.9$  with 188 towers. Each tower is made up of scintillating crystal ( $\text{PbWO}_4$ ) attached to an avalanche photodiode.

### 2.2.5 Electromagnetic Calorimeter

The Electromagnetic Calorimeter (EMCal) is a system of lead scintillator (PbSc) and lead glass (PbGl) detectors with acceptance  $|\eta| < 0.375$  and  $\phi = 90^\circ \times 2$ . Using two different types of detectors allows for a better understanding of systematic uncertainties, and therefore increase confidence of results. There are 6 sectors of PbSc, four in the west arm and two at the top of the east arm. Each sector is made up of 18 supermodules, each supermodule is made up 36 modules, each module is made of four towers, and each tower is made of 66 alternating layers of lead and scintillator that are connected to PMTs via fiber optics. There are 2 sectors of PbGl, each made of 192 supermodules, each supermodule is made of 24 modules, and each module consists of a lead glass crystal attached to a PMT. A diagram of a module of both detector types can be seen in Figure 2.6. The PbGl causes Cherenkov radiation and cannot be used for hadron identification. It does not have as good of timing resolution as the PbSc, but it has better energy resolution and granularity.

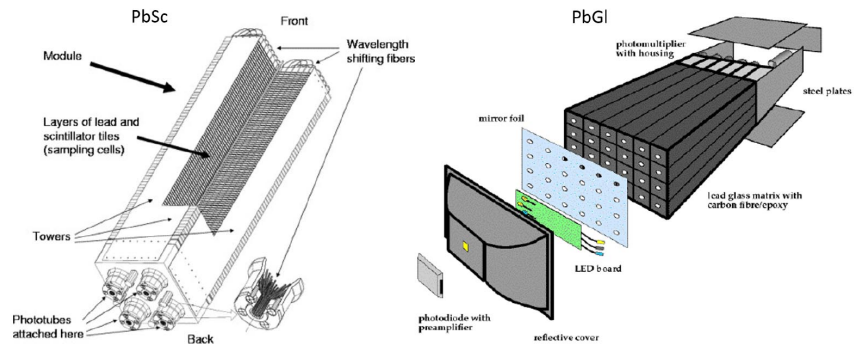


Figure 2.6: (Left) A module of PbSc showing the four towers made up of layers of lead and scintillator. (Right) A module of PbGl showing the 18 towers [16].

Run (Year)	Species	$\sqrt{s_{NN}}$ (GeV)	$\int Ldt$	Sampled Events
1 (2000)	Au + Au	130	$1\mu b^{-1}$	10 M
2 (2001 - 2002)	Au + Au	200	$24\mu b^{-1}$	170 M
	p + p	200	$0.15pb^{-1}$	3.7 B
3 (2002 - 2003)	d + Au	200	$2.74nb^{-1}$	5.5 B
	p + p	200	$0.35pb^{-1}$	6.6 B
4 (2003 - 2004)	Au + Au	200	$241\mu b^{-1}$	1.5 B
	Au + Au	62.4	$9\mu b^{-1}$	58 B
5 (2005)	Cu + Cu	200	$3nb^{-1}$	8.6 B
	Cu + Cu	62.4	$0.19nb^{-1}$	400 M
	Cu + Cu	22.4	$2.7\mu b^{-1}$	9 M
	p + p	200	$3.8 pb^{-1}$	85 B
6 (2006)	p + p	200	$10.7pb^{-1}$	233 B
	p + p	62.4	$0.1S pbS^{-1}$	28 B
7 (2007)	Au + Au	200	$813\mu b^{-1}$	5.1 B
8 (2008)	d + Au	200	$80nb^{-1}$	160 B
	p + p	200	$5.2pb^{-1}$	115 B
9 (2009)	p + p	500	$14pb^{-1}$	308 B
	p + p	200	$16pb^{-1}$	936 B
10 (2010)	Au + Au	200	$1.3nb^{-1}$	7.7 B
	Au + Au	62.4	$0.11nb^{-1}$	700 M
	Au + Au	39	$40\mu b^{-1}$	250 M
	Au + Au	7.7	$0.1pb^{-1}$	1.6 M

Table 2.2: A summary of PHENIX data with the run number and year, the species that was collided, the center of mass pair energy of the collision, the total integrated luminosity, and the number of sampled events [9].

## 3 ANALYSIS AND DISCUSSION I: REACTION PLANE EFFICIENCY AND MONTE CARLO SIMULATIONS

### 3.1 Introduction

The elliptic flow coefficients of the isolated photons, which will be shown in the next chapter, did not look as expected. This lead us to believe that there was an isolation cut efficiency which depends on the event plane. In this Chapter, an assumption of the form for this efficiency is assumed and a rederivation of the two particle correlation function (Equation 1.8) is carried out. The rederived function was then tested using a Monte Carlo simulation. Finally, an isolation cut was added to the simulation to further determine the validity of the event plane isolation cut efficiency.

### 3.2 Derivation of Reaction Plane Efficiency Trigger distribution

Suppose the efficiency has the form

$$\epsilon = \epsilon_0 \left( 1 + 2v_{2E} \cos(2(\phi_T - \Psi)) \right), \quad (3.1)$$

where  $\epsilon_0$  is an overall scale factor efficiency,  $v_{2E}$  is the isolation cut efficiency azimuthal asymmetry coefficient,  $\phi_T$  is the trigger particle's azimuthal angle, and  $\Psi$  is the second order event plane angle. This assumption is reasonable because particles from the underlying event exhibit azimuthal asymmetry with a moderate  $v_2$  and since some of these particles are sampled in the isolation cut, it is reasonable for them to cause an event plane dependent efficiency.

Once this form of this efficiency is assumed, it can be included in the particle's azimuthal anisotropy and takes the form,

$$\begin{aligned}
\frac{dN_{TE}}{d\phi_T} &= \left(1 + 2v_{2T} \cos(2(\phi_T - \Psi))\right) \times \epsilon, \\
&= \left(1 + 2v_{2T} \cos(2(\phi_T - \Psi))\right) \left(1 + 2v_{2E} \cos(2(\phi_T - \Psi))\right) \epsilon_0, \\
&= \epsilon_0 \left(1 + 2v_{2T} \cos(2(\phi_T - \Psi)) + 2v_{2E} \cos(2(\phi_T - \Psi)) + 4v_{2T}v_{2E} \cos^2(2(\phi_T - \Psi))\right), \\
&= \epsilon_0 \left(1 + 2(v_{2T} + v_{2E}) \cos(2(\phi_T - \Psi)) + 4v_{2T}v_{2E} \cos^2(2(\phi_T - \Psi))\right).
\end{aligned} \tag{3.2}$$

Equation 3.2 shows that when the trigger  $\Delta\phi$  distribution is fit to  $1 + 2v_2 \cos(2\Delta\phi)$ , the  $v_2$  that is measured not just  $v_{2T}$  but  $v_{2T} + v_{2E}$ . There is also cosine squared term that may have a small effect of the fit.

### 3.3 Monte Carlo Confirmation of Reaction Plane Efficiency Trigger distribution

In order to test this function, a simple Monte Carlo (MC) simulation was made to generate random  $\Delta\phi$  and event plane,  $\phi_{EP}$ , angles. The  $\Delta\phi$  angles were distributed according to

$$1 + 2v_2 \cos(2(\Delta\phi)), \tag{3.3}$$

where  $v_2$  is an input coefficient that can be  $-0.5 \geq v_2 \geq 0.5$ . The event plane angles were generated uniformly according to  $\Psi_2$  in Equation 1.6. The  $\Delta\phi$  was accepted if  $\phi_T = \Delta\phi + \phi_{EP}$  was in the PHENIX acceptance (Equation 2.1) and it passed a MC test. The MC test consisted of generating a random number,  $\Upsilon$ , such that  $0 \leq \Upsilon \leq 1$  according to

$$\Upsilon = \frac{1 + 2v_{2E} \cos(2(\Delta\phi))}{1 + 2v_{2E}}, \tag{3.4}$$

where  $v_{2E}$  is an input efficiency value. If  $\Upsilon$  is greater than a uniform random number between zero and one then the  $\Delta\phi$  passes the MC test and is accepted. When this is done a

large number of times, it generates a particle distribution which must then be acceptance corrected.

### 3.3.1 Acceptance Correction

As seen in Chapter 1 (Figure 1.8), the peaks in the two-particle correlation functions are caused by jets. There are also underlying event particles (the background) that must be subtracted to get this true jet distribution. This data was taken by STAR, the other operating experiment at RHIC. STAR has full azimuthal and a long rapidity acceptance. PHENIX does not have full azimuthal coverage so the data must be acceptance corrected.

PHENIX does not have full acceptance because the central magnet limits where the detectors are placed. Since the azimuthal coverage of one particle is known, the correction for the two-particle correlations is obtained through a four step process:

- plot  $\phi_1$  versus  $\phi_2$  (Figure 3.1a),
- transform this into  $\phi_1$  versus  $\Delta\phi = \phi_1 - \phi_2$  (Figure 3.1b),
- project this histogram onto the  $\Delta\phi$  axis to obtain a one dimensional acceptance as a function of  $\Delta\phi$  ( $Acc(\Delta\phi_{12})$ ) (Figure 3.1c),
- divide the pair distribution by  $Acc(\Delta\phi_{12})$  to obtain the corrected two-particle correlation, then

$$\frac{dN_{real}^{AB}}{d\Delta\phi_{AB}} = \frac{1}{Acc(\Delta\phi_{AB})} \frac{dN_{raw}^{AB}}{d\Delta\phi_{AB}}. \quad (3.5)$$

The acceptance function has a maximum at  $\Delta\phi_{12} = 0$ , when the particle pairs are aligned, and a minimum at  $\Delta\phi_{12} = \pi/2$ , when the pairs are perpendicular to one another.

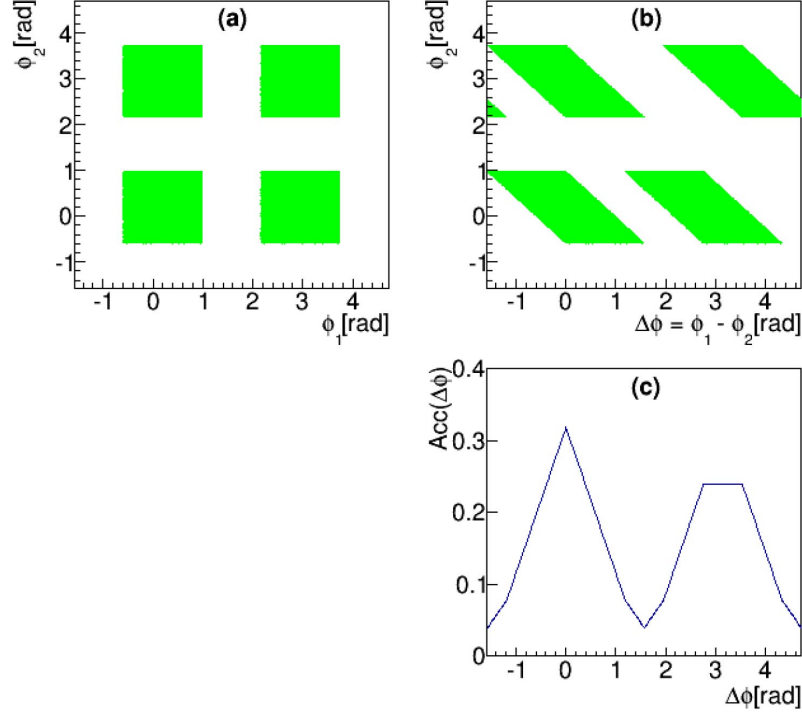


Figure 3.1: (a)  $\phi_1$  vs  $\phi_2$  for the pairs in the PHENIX acceptance. (b)  $\phi_1$  vs  $\Delta\phi_{12}$  (c)  $Acc(\Delta\phi_{12})$  is obtained by projecting of  $\phi_1$  vs  $\Delta\phi_{12}$  onto the  $\Delta\phi_{12}$  axis [9].

Here,  $\phi_1 = \phi_T$  and  $\phi_2 = \phi_{EP}$ . When this correction is done for the trigger azimuthal angles (Figure 3.2a) and the reaction plane angles (Figure 3.2b), it generates the acceptance function shown in Figure 3.2c.

The trigger particle's  $\Delta\phi$  distribution is then divided by this to obtain the acceptance corrected distribution (Figure 3.2d). The red line is the fit according to

$$\frac{dN}{d\Delta\phi} = \mathcal{A}(1 + 2\mathcal{B} \cos(2(\Delta\phi)) + 4C \cos^2(2(\Delta\phi))), \quad (3.6)$$

where  $\mathcal{A}$ ,  $\mathcal{B}$ , and  $C$  are fit parameters and  $\Delta\phi = \phi_T - \phi_{EP}$ . This is the same form as Equation 3.2 with an overall normalization factor,  $\mathcal{A}$ . The fit values demonstrate  $\mathcal{B} = v_{2T} + v_{2E}$  and  $C = v_{2T}v_{2E}$ . One can also see in Figure 3.2d that the maxima of the

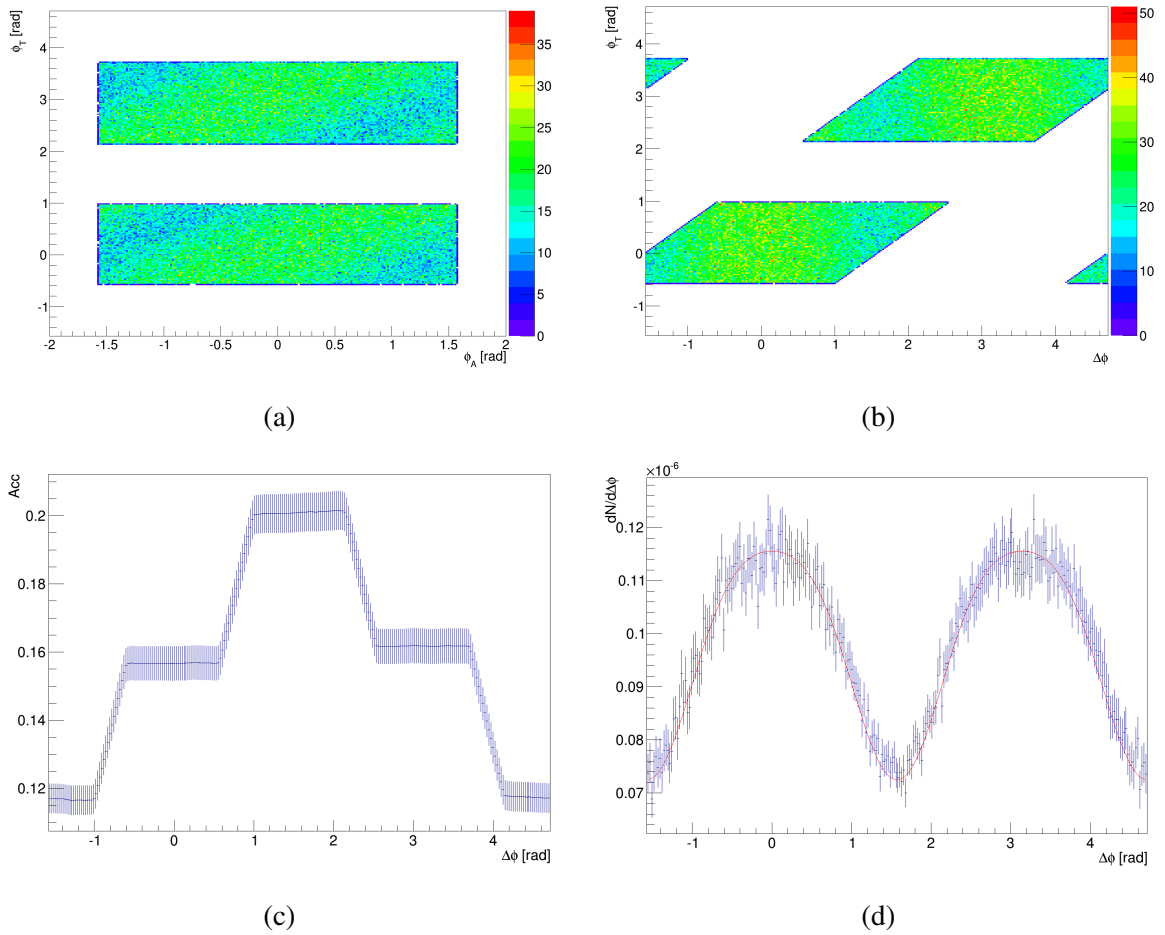


Figure 3.2: (a) Trigger angle versus reaction plane angle. (b) Trigger angle versus  $\Delta\phi = \phi_T - \phi_{EP}$ . (c) Pair acceptance function for the accepted trigger azimuthal angles and reaction plane angles. (d) Acceptance corrected trigger-reaction plane correlation.

distribution is broader than a typical cosine curve, this is caused by the higher order term ( $\cos^2(2\Delta\phi)$ ). This justifies assuming there is a reaction plane cone efficiency of the form of Equation 3.1 is consistent with the simulation. This method can be extended to determine which  $v_2$  parameter, or combination thereof, should be used for the direct photon-hadron correlation.

### 3.4 Derivation of the Two Particle Correlation Function with Reaction Plane Efficiency

In order to obtain a correlation, particles associated with the trigger particles must be generated. These associated particles have the same event plane angle and are generated the same way as the trigger particles but are not subject to the MC test. They are accepted if they are in the PHENIX azimuthal acceptance. The distribution of the associated particles must be acceptance corrected just like the trigger distribution. Once it is acceptance corrected, in order to determine if the method of accepting associated particles is admissible, it is fit according to

$$\frac{dN}{d\Delta\phi} = \mathcal{D}(1 + 2\mathcal{E} \cos(2(\Delta\phi))), \quad (3.7)$$

where  $\mathcal{D}$  and  $\mathcal{E}$  are fit parameters and  $\Delta\phi = \phi_A - \phi_{EP}$ . Equation 3.7 is used because the particles are generated according to Equation 3.3. Figure 3.3 shows an associated particle distribution with the fit (red line). One can see that the red line matches the distribution well.

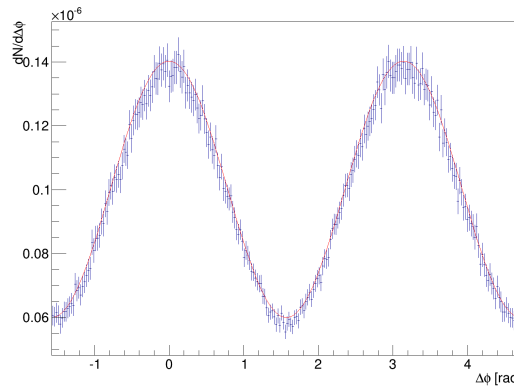


Figure 3.3: Acceptance corrected associated-reaction plane correlation.

Now that trigger particles with a reaction plane cone efficiency and associated particles have been generated, the trigger-associated particle (T-A) correlation function is determined by:

$$\frac{dN_{TA}}{d\Delta\phi} = \int d\phi_T \int d\phi_A \int d\Psi acc(\phi_T)acc(\phi_A) \frac{dN_{TE}}{d\phi_T} \frac{dN_A}{d\phi_A} \delta(\Delta\phi - (\phi_T - \phi_A)), \quad (3.8)$$

where the integrals are over the full azimuth,  $N_{TA}$  is the number of trigger-associated particle pairs,  $acc(\phi_T)$  and  $acc(\phi_A)$  are the raw pair acceptance functions of the trigger and associated particles, respectively,  $dN_{TE}/d\phi_T$  is the trigger distribution with the efficiency incorporated (Equation 3.2), and  $dN_A/d\phi_A$  is the azimuthal distribution of the associated particles, defined by

$$\frac{dN_A}{d\phi_A} = 1 + 2v_{2A} \cos(2(\phi_A - \Psi)), \quad (3.9)$$

It follows that,

$$\begin{aligned} \frac{dN_{TE}}{d\phi_T} \frac{dN_A}{d\phi_A} &= \\ &= \epsilon_0 (1 + 2v_{2E} \cos(2(\phi_T - \Psi))) (1 + 2v_{2T} \cos(2(\phi_T - \Psi))) (1 + 2v_{2A} \cos(2(\phi_A - \Psi))) \\ &= \epsilon_0 (1 + 2v_{2T} \cos(2(\phi_T - \Psi)) + 2v_{2A} \cos(2(\phi_A - \Psi)) + 2v_{2E} \cos(2(\phi_T - \Psi)) \\ &\quad + 4v_{2T}v_{2A} \cos(2(\phi_T - \Psi)) \cos(2(\phi_A - \Psi)) + 4v_{2E}v_{2A} \cos(2(\phi_T - \Psi)) \cos(2(\phi_A - \Psi)) \\ &\quad + 4v_{2T}v_{2E} \cos^2(2(\phi_T - \Psi)) + 8v_{2T}v_{2A}v_{2E} \cos^2(2(\phi_T - \Psi)) \cos(2(\phi_A - \Psi))). \end{aligned} \quad (3.10)$$

Implementation of a convenient trigonometric identity,

$$\cos(a - b) = \cos(a) \cos(b) + \sin(a) \sin(b), \quad (3.11)$$

separates the cosines so the integral (Equation 3.8) can be expanded. It then reads:

$$\begin{aligned}
\frac{dN_{TA}}{d\Delta\phi} = & \int d\phi_T \int d\phi_A \int d\Psi \epsilon_0 \delta(\Delta\phi - (\phi_T - \phi_A)) acc(\phi_T) acc(\phi_A) \\
& \left( 1 + 2v_{2T} \left( \cos(2\phi_T) \cos(2\Psi) + \sin(2\phi_T) \sin(2\Psi) \right) \right. \\
& + 2v_{2A} \left( \cos(2\phi_A) \cos(2\Psi) + \sin(2\phi_A) \sin(2\Psi) \right) \\
& + 2v_{2E} \left( \cos(2\phi_T) \cos(2\Psi) + \sin(2\phi_T) \sin(2\Psi) \right) \\
& + 4v_{2T}v_{2A} \left( \cos(2\phi_T) \cos(2\phi_A) \cos^2(2\Psi) + \sin(2\phi_T) \sin(2\phi_A) \sin^2(2\Psi) \right. \\
& \quad + \cos(2\phi_T) \sin(2\phi_A) \sin(2\Psi) \cos(2\Psi) \\
& \quad \left. + \sin(2\phi_T) \cos(2\phi_A) \sin(2\Psi) \cos(2\Psi) \right) \\
& + 4v_{2A}v_{2E} \left( \cos(2\phi_T) \cos(2\phi_A) \cos^2(2\Psi) + \sin(2\phi_T) \sin(2\phi_A) \sin^2(2\Psi) \right. \\
& \quad + \cos(2\phi_T) \sin(2\phi_A) \sin(2\Psi) \cos(2\Psi) \\
& \quad \left. + \sin(2\phi_T) \cos(2\phi_A) \sin(2\Psi) \cos(2\Psi) \right) \\
& + 4v_{2T}v_{2E} \left( \cos^2(2\phi_T) \cos^2(2\Psi) + \sin^2(2\phi_T) \sin^2(2\Psi) \right. \\
& \quad + 2 \sin(2\phi_T) \cos(2\phi_T) \sin(2\Psi) \cos(2\Psi) \\
& \quad \left. + 8v_{2T}v_{2A}v_{2E} \left( \cos^2(2\phi_T) \cos(2\phi_A) \cos^3(2\Psi) + \sin^2(2\phi_T) \sin(2\phi_A) \sin^3(2\Psi) \right. \right. \\
& \quad + \sin^2(2\phi_T) \cos(2\phi_A) \sin^2(2\Psi) \cos(2\Psi) \\
& \quad + \cos^2(2\phi_T) \sin(2\phi_A) \sin(2\Psi) \cos^2(2\Psi) \\
& \quad + 2 \cos^2(2\phi_T) \sin(2\phi_T) \cos(2\phi_A) \sin(2\Psi) \cos^2(2\Psi) \\
& \quad \left. \left. + 2 \sin(2\phi_T) \cos(2\phi_T) \sin(2\phi_A) \sin^2(2\Psi) \cos(2\Psi) \right) \right). 
\end{aligned} \tag{3.12}$$

This daunting integral is easily tackled because the  $\Psi$  integral will equal zero for the functions periodic in  $\Psi$  ( $\sin(2\Psi)$  and  $\cos(2\Psi)$ ). This vastly simplifies Equation 3.12 to

$$\begin{aligned}
\frac{dN_{TA}}{d\Delta\phi} = & \int d\phi_T \int d\phi_A \int d\Psi \epsilon_0 \delta(\Delta\phi - (\phi_T - \phi_A)) acc(\phi_T) acc(\phi_A) \\
& \left( 1 + 4v_{2T}v_{2A} \left( \cos(2\phi_T) \cos(2\phi_A) \cos^2(2\Psi) + \sin(2\phi_T) \sin(2\phi_A) \sin^2(2\Psi) \right) \right. \\
& + 4v_{2A}v_{2E} \left( \cos(2\phi_T) \cos(2\phi_A) \cos^2(2\Psi) + \sin(2\phi_T) \sin(2\phi_A) \sin^2(2\Psi) \right) \\
& \left. + 4v_{2T}v_{2E} \left( \cos^2(2\phi_T) \cos^2(2\Psi) + \sin^2(2\phi_T) \sin^2(2\Psi) \right) \right). 
\end{aligned} \tag{3.13}$$

The  $\Psi$  integrals over sine and cosine squared give  $\pi/2$  while over 1 gives  $\pi$ . Using this result and Equation 3.11 transforms Equation 3.13 into

$$\begin{aligned}
\frac{dN_{TA}}{d\Delta\phi} = & \int d\phi_T \int d\phi_A \epsilon_0 \delta(\Delta\phi - (\phi_T - \phi_A)) acc(\phi_T) acc(\phi_A) \pi \\
& \left( 1 + 2v_{2T}v_{2A} \left( \cos(2\phi_T) \cos(2\phi_A) + \sin(2\phi_T) \sin(2\phi_A) \right) \right. \\
& + 2v_{2A}v_{2E} \left( \cos(2\phi_T) \cos(2\phi_A) + \sin(2\phi_T) \sin(2\phi_A) \right) \\
& \left. + 2v_{2T}v_{2E} \left( \cos^2(2\phi_T) + \sin^2(2\phi_T) \right) \right).
\end{aligned} \tag{3.14}$$

Since  $\sin^2(a) + \cos^2(a) = 1$  and using Equation 3.11 once again,

$$\begin{aligned}
\frac{dN_{TA}}{d\Delta\phi} = & \int d\phi_T \int d\phi_A \epsilon_0 \delta(\Delta\phi - (\phi_T - \phi_A)) acc(\phi_T) acc(\phi_A) \pi \\
& \left( 1 + 2v_{2T}v_{2A} \cos(2(\phi_T - \phi_A)) + 2v_{2A}v_{2E} \cos(2(\phi_T - \phi_A)) + 2v_{2T}v_{2E} \right).
\end{aligned} \tag{3.15}$$

Carrying out the  $\delta$  function integral gives the final result,

$$\begin{aligned}
\frac{dN_{TA}}{d\Delta\phi} = & Acc(\phi_T) Acc(\phi_A) \pi \epsilon_0 \left( 1 + 2v_{2T}v_{2A} \cos(2(\Delta\phi)) + 2v_{2A}v_{2E} \cos(2(\Delta\phi)) + 2v_{2T}v_{2E} \right) \\
= & Acc(\phi_T) Acc(\phi_A) \pi \epsilon_0 \left( 1 + 2v_{2T}v_{2E} + 2(v_{2T}v_{2A} + v_{2A}v_{2E}) \cos(2(\Delta\phi)) \right).
\end{aligned} \tag{3.16}$$

This shows that in the  $\gamma_{dir}$ -h correlation the correct  $v_2$  value to use is not  $v_{2A}v_{2T}$ , but  $v_{2A}(v_{2T} + v_{2E})$ . There are also no higher order cosine terms like in the trigger  $\Delta\phi$  distribution (Equation 3.2). The first term now depends on  $v_{2T}v_{2E}$ , it is not just a constant value of one. This can now be used to fit the T-A correlation with the form:

$$\frac{dN_{TA}}{d\Delta\phi} = \mathcal{F}(\mathcal{G} + 2\mathcal{H} \cos(2(\Delta\phi))). \quad (3.17)$$

The fit parameter  $\mathcal{F}$  is an overall normalization factor that includes information about  $Acc$  and  $\epsilon_0$  while  $\Delta\phi = \phi_T - \phi_A$ . The other parameters as defined as

$$\begin{aligned} \mathcal{G} &= 1 + 2v_{2T}v_{2E}, \\ \mathcal{H} &= v_{2T}v_{2A} + v_{2A}v_{2E} \\ &= v_{2A}(v_{2T} + v_{2E}). \end{aligned} \quad (3.18)$$

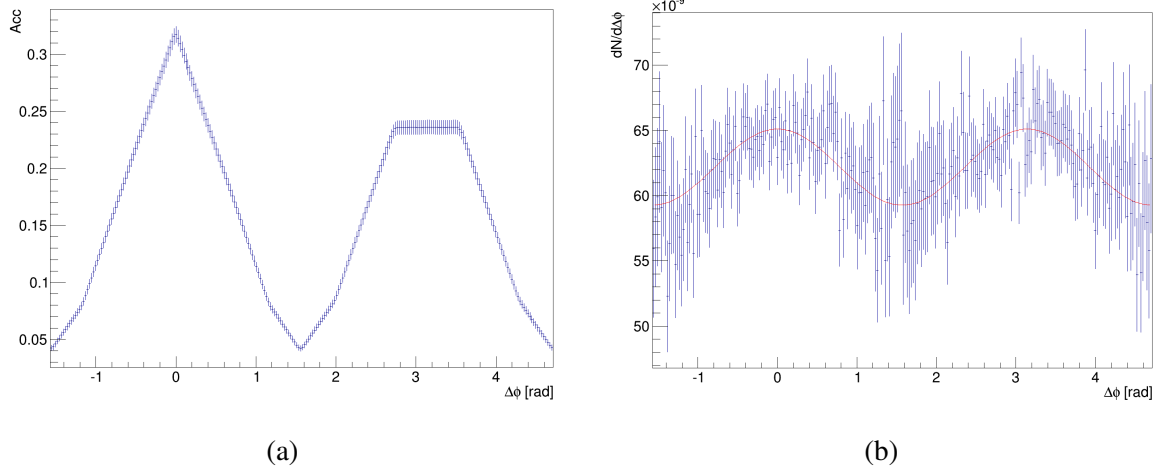


Figure 3.4: (a) Pair acceptance function for the accepted trigger azimuthal angles and accepted associated particles' azimuthal angles. (b) Acceptance corrected trigger-associated particle correlation.

The acceptance function (shown in Figure 3.4a) looks as anticipated (Figure 3.1c). Figure 3.4b shows the T-A correlation with the fit according to Equation 3.17. The output fit parameters match the input  $v_2$  values according to Equation 3.18 is correct. This confirms the correct amplitudes to use in the  $\gamma_{dir}$ -h correlation (Equation 1.8) is not just  $v_{2A}v_{2T}$  but  $v_{2A}(v_{2T} + v_{2E})$ . This leads to another question, what is  $v_{2E}$  and how is it found in the data? To answer these questions, the MC simulation should be made more sophisticated to include an isolation cut.

### 3.5 Confirmation of the Isolation Cut Reaction Plane Efficiency

#### 3.5.1 Isolation Cut

The method behind the isolation cut was briefly discussed in Chapter 1. This method is desired because it removes decay photons from the outgoing particle distribution. Each photon in each event has a cone around it with a radius according to

$$R_{cone} = \sqrt{(\Delta\phi)^2 + (\Delta\eta)^2}. \quad (3.19)$$

The energy inside the cone is then measured, if it is smaller than the threshold energy ( $E_{TH}$ ), the photon is isolated. If the energy is greater, the photon is not isolated and probably originated from a decay. This process is depicted in Figure 3.5.

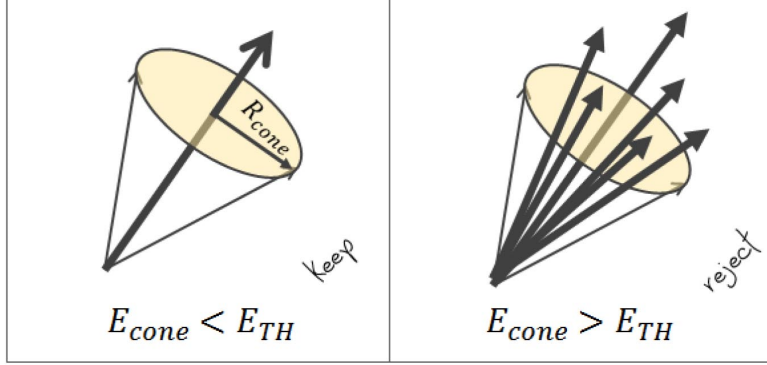


Figure 3.5: Definition of the isolation cut method for finding isolated photons. The black arrows are particles inside the cone. [9]

There is no  $\eta$  dependence needed in the simulation because flow only depends on the azimuthal angle of the particle. This makes a one dimensional cut. In a more sophisticated simulation we generate the reaction plane angles and associated  $\Delta\phi$  values the same way it is done in the simple simulation. The trigger  $\Delta\phi$  is subject to a different test this time. Once it is determined to be in the acceptance, a random number is generated according to a Poisson distribution with the mean

$$P_{mean} = 10(1 + 2v_{2U} \cos(2(\phi_T - \phi_{RP}))) \frac{\int_{\phi_T-0.2}^{\phi_T+0.2} (1 + 2v_{2T} \cos(2(\phi_T - \phi_{RP}))) d(\phi_T - \phi_{RP})}{0.4}. \quad (3.20)$$

If this number is less than a cut off value, the trigger is accepted. The cut value is determined such that the number of accepted triggers is 70% of the total generated triggers. Mathematically, this is

$$N_{Poisson} \leq N_{cut} = \frac{\text{accepted triggers}}{\text{all triggers}} \approx 0.7. \quad (3.21)$$

Poissonian numbers were used because they emulate the cone energy distributions observed in the data. This exact form for the mean was chosen for a few reasons, the

integral provides for a one dimensional isolation cut with a width of 0.4, the efficiency is given by the term before the integral,  $v_{2U}$  is an input value that is similar to the underlying event  $v_2$ , and the factor of 10 ensures the distribution is similar to the energy distribution of the cones in the data (Figure 5.1). The value of 70% was chosen to resemble the average efficiency of the cones in the data, described in Section 5.1.

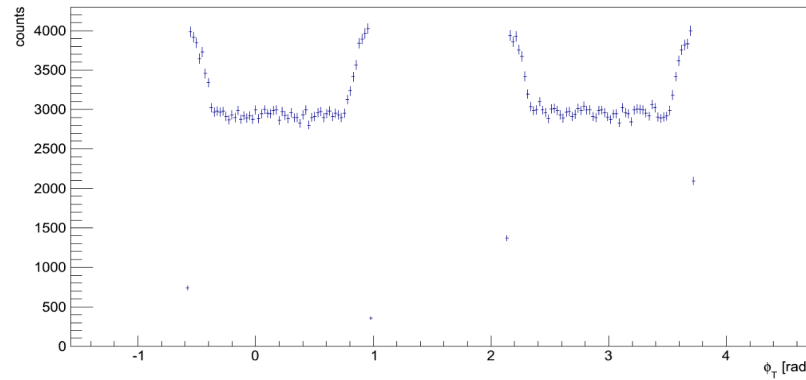


Figure 3.6: Accepted triggers when isolation cut is applied.

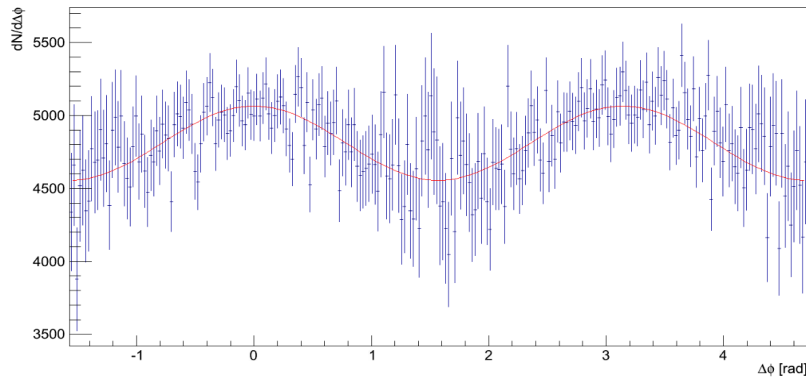


Figure 3.7: Trigger-associated particle correlation when the isolation cut is applied.

The accepted trigger  $\phi$  values can be seen in Figure 3.6. The peaks on the edges of the acceptance are caused by an increase in the number of accepted triggers due to a small

integral value that drives down the  $P_{mean}$  (See Equation 3.20). Figure 3.7 shows the triggers'  $\Delta\phi = \phi_T - \phi_{RP}$  distribution once it was divided by the acceptance. It is similar to the distribution generated by the simple MC simulation and is fit with the same function (Equation 3.6).

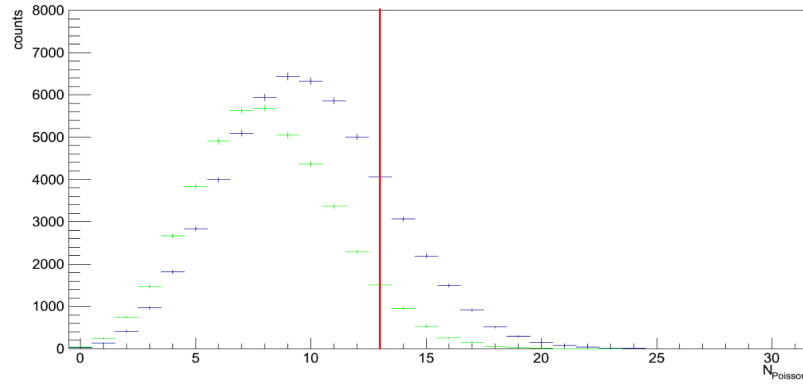


Figure 3.8:  $N_{Poisson}$  distributions for cones in (blue curve) and out (green curve) of reaction plane. Ratio of the integral from 0 to the red line to the total integral was taken to find the efficiency. Doing this for the blue curve produces the efficiency  $\Delta\phi$  bin centered around 0. The green curve produces the efficiency  $\Delta\phi$  bin centered around 1.25.

The cone's Poisson distributions is shown in Figure 3.8 for two  $\Delta\phi$  bins. The blue line is from particles that are in the event plane ( $\Delta\phi \approx 0$ ) the green line is the particles that are out of the plane ( $\Delta\phi \approx 1.25$ ). This shows that there are more particles with high energy in the plane.

To get the cone efficiency, the ratio of the total integral to the integral taken from 0 to  $N_{cut}$  (red line in Figure 3.8) was taken for ten  $\Delta\phi$  bins as shown in Figure 3.9. This is then fit according to Equation 3.7. This fit yields a value for  $v_{2E}$ .

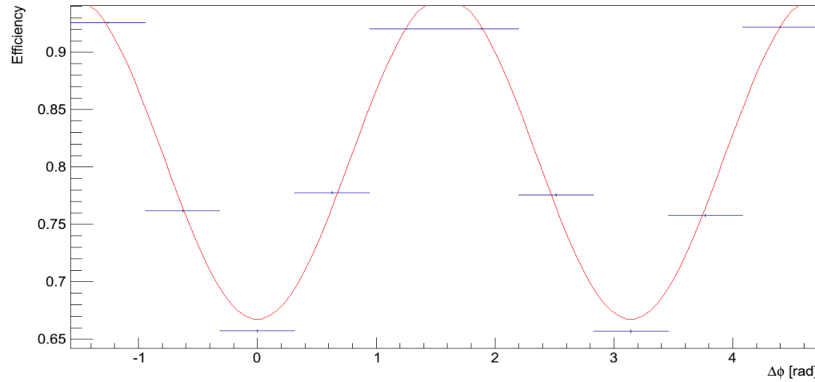


Figure 3.9: Cone efficiency as a function of  $\Delta\phi$ .

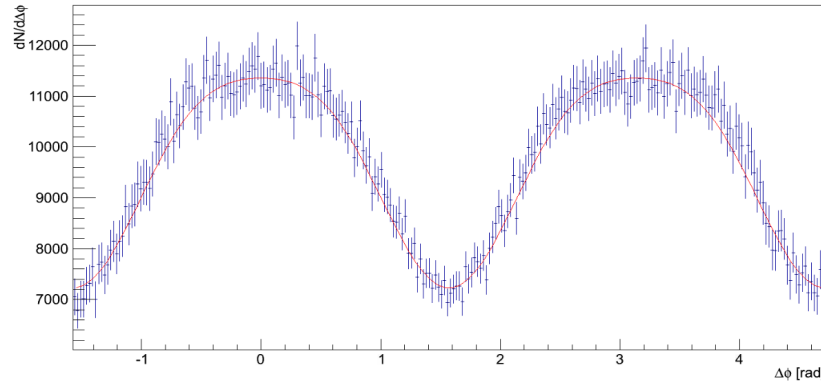


Figure 3.10: Trigger-reaction plane correlation for sophisticated MC simulation..

Figure 3.10 shows the trigger  $\Delta\phi$  distribution with the fit according to Equation 3.6.

The fit parameter  $\mathcal{B} = v_{2T} + v_{2E}$  was measured, and the fit  $v_{2E}$  from Figure 3.9 was subtracted in order to determine  $v_{2T}$ . This value matched the input  $v_2$  for a myriad of combinations of input  $v_2$  and  $v_{2U}$ . The fit parameters are always consistent with the derived fit parameters presented in this Chapter. This process is carried out in the data and can be seen in Section 5.1.

## 4 ANALYSIS AND DISCUSSION II: MEASUREMENT OF ELLIPTIC FLOW COEFFICIENTS OF ISOLATED $\gamma$ AND $\pi^0$ IN PHENIX RUN 10

### 4.1 Data Selection

The data used in this thesis were minimum bias events detected by PHENIX. A minimum bias event consists of coincidence in both the North and South modules of the BBC and least one neutron's energy deposited in one of the ZDC modules. A cut was applied such that the z-vertex of each collision is within 30 cm of the nominal collision point in order to reduce the effects of limited  $\eta$  acceptance effect of PHENIX.

There are several criteria for photon selection: they must have  $p_T \geq 2.5$  GeV/c, pass a  $\chi^2$  cut based on its cluster shape in the EMCAL, pad chamber/EMCAL comparison, hot and dead tower removal, and cluster removal from the edge of the EMCAL. A cluster is caused by an electromagnetic shower inside the EMCAL. It is defined by hits on several towers with the largest signal in the center. Photons have a characteristic cluster shape, each detected cluster shape is compared to this characteristic shape and identified as a photon if  $\chi^2 < 3$ . This cut removes signals from neutral hadrons because they cause a different cluster shape. Electrons do not affect this cut because their signals are removed by matching tracks with the Ring Imaging Cherenkov (RICH) detector. The PC/EMCAL comparison consists of removing a cluster in the EMCAL if it is within  $\phi > 0.01$  rad and  $z > 5$  cm of the pad chamber. This ensures that a charged particle has not contaminated the photon cluster.

Towers in the EMCAL can be lost, either by going dead (dead towers) or being constantly on (hot towers). This can affect the cluster measurement either by losing or gaining signals. Towers are hot if their number of hits is  $5\sigma$  above the average of the other towers. Clusters that occur in these towers are not accepted. Clusters that occur on the

edges of the EMCal are also not accepted because part of their energy is probably deposited outside of the detector. Recalibration of the EMCal is described in [9].

Neutral pions with  $p_T \geq 4$  GeV/c are used for the  $\pi^0$  analysis. Most of the time, almost 99%,  $\pi^0$  particles decay into two photons[1]. Pions are detected by reconstructing this decay through calculation of the invariant mass of a pair of photons and comparing it to the  $\pi^0$  mass. The invariant mass squared of the photons is

$$m_{\gamma_1\gamma_2}^2 = 2E_{\gamma_1}E_{\gamma_2}(1 - \cos \Phi), \quad (4.1)$$

where  $E_\gamma$  is the energy of the photon, and  $\Phi$  is the their separation angle in both azimuth and pseudorapidity. The finite detector resolution causes the photon's invariant mass to form a Gaussian with the peak at the mass of the  $\pi^0$ , 0.134 GeV [1]. If the invariant mass is  $0.12 < m_{\gamma_1\gamma_2} < 0.16$  GeV (vertical orange lines in Figure 4.1) then the pairs come from a decay originate from a  $\pi^0$ . This range was used to in order to have a high signal-to-background ratio [9]. The black lines below the gaussian curves in the Figure 4.1 are linear fits to the background. Cuts on energy of the photons are defined in [9]. Outside of these thresholds, the photon invariant mass is unlikely to yield a  $\pi^0$ . In this analysis, the  $\pi^0$  must have  $p_T \geq 4$  GeV/c.

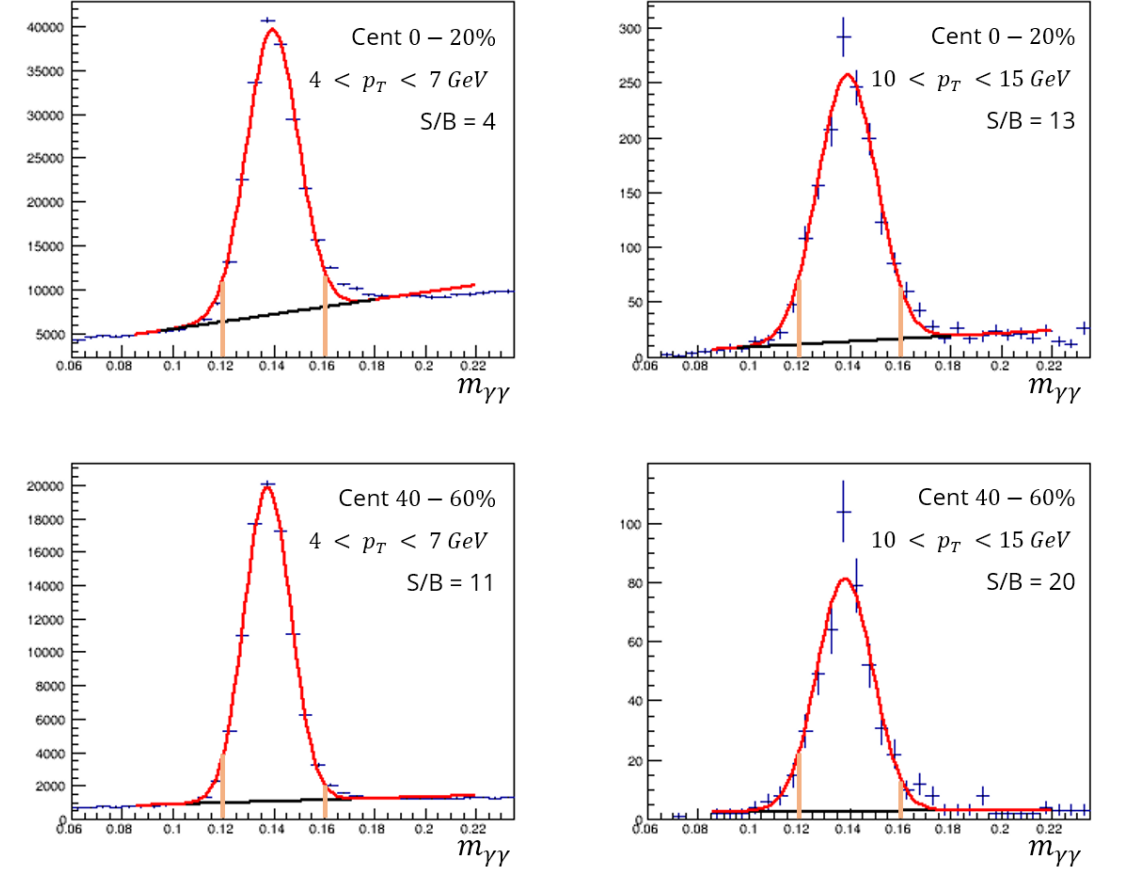


Figure 4.1: Invariant mass of photon pairs, used for  $\pi^0$  selection. The top plots are 0-20% centrality with two different  $p_T$  bins. The bottom plots are 40-60% centrality with the same  $p_T$  bins as the top plots. Between the orange lines, the photons decayed from a  $\pi^0$  as described in the text [9].

#### 4.1.1 Isolation Cut

Isolation cuts are commonly used in p+p collisions but less so in Au+Au collisions because of their high multiplicity. A study was done by [9] which varied the isolation cut in order to minimize the statistical uncertainties in the  $\gamma_{dir}$ -h correlations. It was found

that the optimal threshold energy ( $E_{threshold}$ ) of the cone depends on the photon's energy ( $E_\gamma$ ) according to Equation 4.2.

$$E_{threshold} = aE_\gamma + b. \quad (4.2)$$

Parameter  $a$  is a factor that is standard in p + p collisions and  $b$  is roughly the average energy random cones, the underlying event energy. It varies with centrality because the multiplicity varies. This leads to the minimization of uncertainties to determine the parameters  $a$  and  $b$ , the results of which are shown in Table 4.1 [9].

Centrality (%)	$R_{cone}$	$a$	$b$
0 - 20	0.1	0.1	2.0
20 - 40	0.2	0.1	4.0
40 - 60	0.2	0.1	2.0
60 - 92	0.3	0.1	1.0

Table 4.1: Isolation cut paramters  
for all centralities

#### 4.1.2 Acceptance Correction

In the experiment, the acceptance function is perturbed run-by-run by dead regions in the detectors. Dead regions are caused by any number of reasons, from a wire being disconnected to the detector's electronics needing to be restarted. In order to account for this in the data, correlations between particles in different events close in time are measured because there is no physics correlation between these mixed pairs so any

correlation they exhibit must come from the acceptance. This definition of the acceptance function is:

$$Acc(\Delta\phi_{AB}) = \frac{2\pi}{\int \frac{dN_{mix}^{AB}}{d\Delta\phi_{AB}} d\Delta\phi_{AB}} \frac{dN_{mix}^{AB}}{d\Delta\phi_{AB}}, \quad (4.3)$$

where  $N^{AB}$  is the number of particle pairs of type A and B and the factor of  $2\pi$  provides for the full azimuth normalization. The pair distribution is then divided by the acceptance function to obtain the real acceptance corrected particle distribution as described by Equation 3.5. This is done for both two-particle correlations ( $\phi_T$  with  $\phi_A$ , Figure 3.1) as well as trigger or associated particle distributions (( $\phi_T$  or  $\phi_A$  with  $\Psi$ , Figure 3.2).

## 4.2 Extracting $v_2$

Once the data is selected, the particles' ( $\gamma$  or  $\pi^0$ ) yield in bins of transverse momentum is plotted versus  $\Delta\phi = \phi_T - \phi_{EP}$  and event plane, called the foreground. Each reaction plane and each  $p_T$  bin is then projected onto the  $\Delta\phi$  axis. This projection is then normalized. The background particles' histogram is then projected in the same region and normalized. Here, normalized implies the each bin's contents were divided by the total histogram content. Finally, it is fit with

$$\frac{dN}{d\Delta\phi} = 1 + 2\mathcal{E} \cos(2(\Delta\phi)), \quad (4.4)$$

where fit parameter  $\mathcal{E}$  is the extracted  $v_2$  parameter. This process is then repeated for all reaction planes and all  $p_T$  bins.

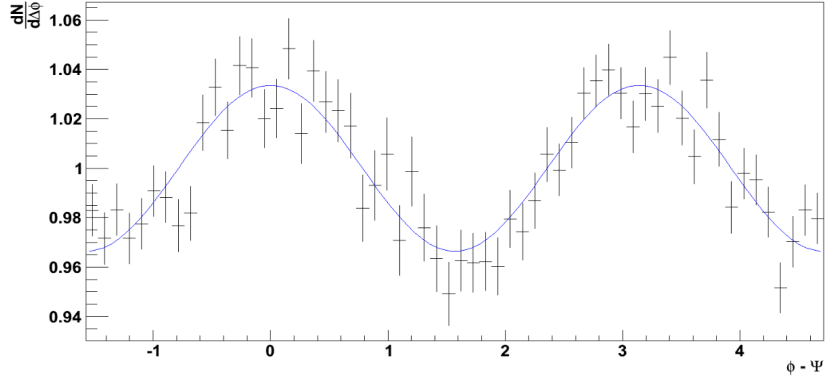


Figure 4.2: Example  $\Delta\phi$  distribution for 40-60% centrality isolated photons for reaction plane BBC N with  $7.0 < p_T < 9.0$  GeV/c. The  $v_2$  value is obtained by fitting with 4.4 (the blue line).

#### 4.2.1 Event Plane Resolution

Due to the finite number of particles that make up the event plane, there must be a factor that includes this property. This factor is called the event plane resolution. The correction is

$$v_2 = \frac{v_2^{raw}}{\langle \cos(2(\Psi_2 - \Psi_{RP})) \rangle}, \quad (4.5)$$

where  $v_2^{raw}$  is the raw measured elliptic flow coefficient and

$$\langle \cos(2(\Psi_2 - \Psi_{RP})) \rangle = \sqrt{\langle \cos(2(\Psi_2^S - \Psi_2^N)) \rangle}. \quad (4.6)$$

Here,  $\Psi_2^S$  and  $\Psi_2^N$  are the second order event planes measured by the North and South BBC modules, respectively. The North and South event planes are used because the true reaction plane cannot be determined with full certainty. The resolution correction always increases  $v_2$  because the average of the cosine is less than one [15]. Figure 4.3 shows the azimuthal asymmetry distribution of the two event planes. The asymmetry can be fit

according to Equation 4.4 to get the amplitude because Equation 1.4 shows that the average of the cosine is half the amplitude of the azimuthal asymmetry as a function of  $\Delta\phi$  or the average could be determined directly. The resolution values used to correct Figures 4.4 - 4.11 are directly calculated.

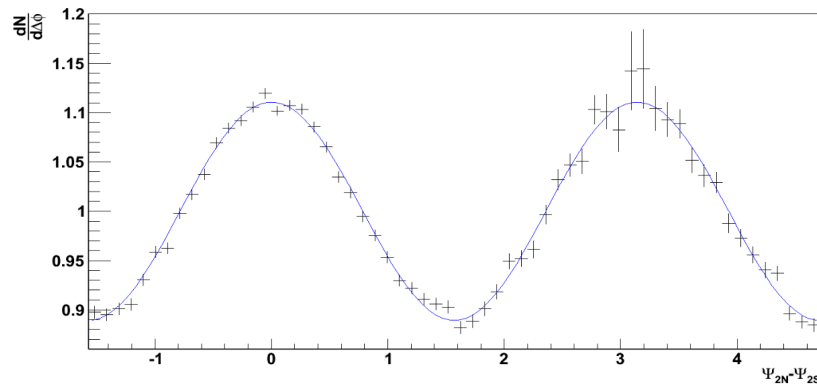


Figure 4.3: Azimuthal distribution of BBC for the most central events. The fit can be used to obtain the resolution, but it is not used in this analysis.

### 4.3 Measurement of $v_{2e\text{ffective}}$

The resolution corrected  $v_{2e\text{ffective}}$ , (the quantity that should be used for the subtraction in two-particle correlation analyses), for isolated photons as a function of  $p_T$  for four centralities is shown in Figures 4.4 - 4.7. The isolated  $\pi^0 v_2$  versus  $p_T$  can be seen in Figures 4.8 - 4.11. There are three different reaction planes, all detected by the BBC, the independent North (BBC N) and South (BBC S) and the average of the two (BBCNS). The BBCNS has the highest resolution because it embodies the most particles causing it to be closest to the reaction plane. Each point on these plots was generated by fitting Equation 4.4 to the particles' distribution as described in Section 4.2. The error bars in the Figures are statistical only, systematics are discussed in Section 4.4.

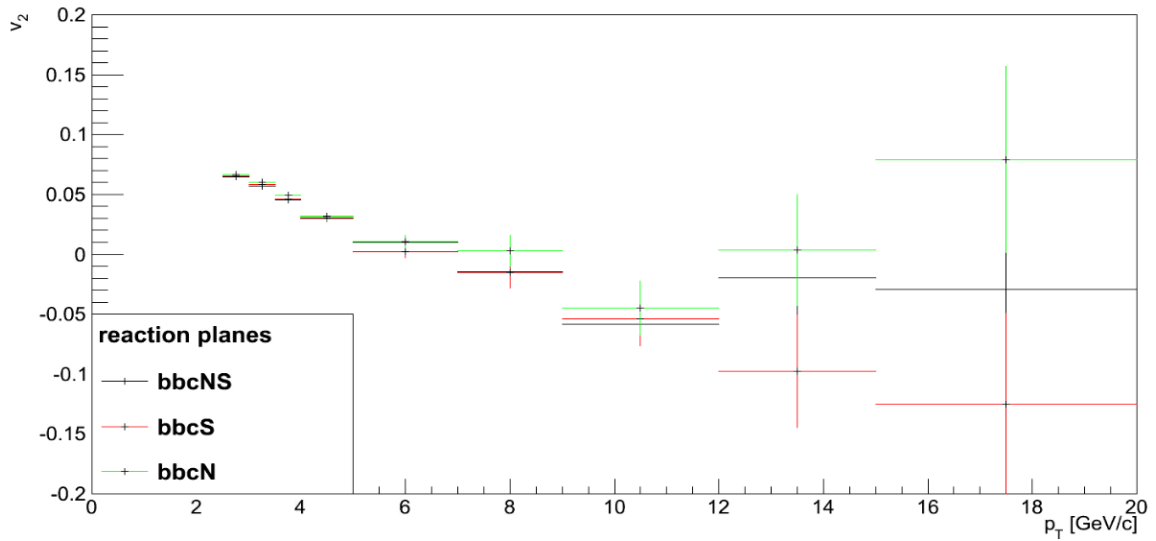
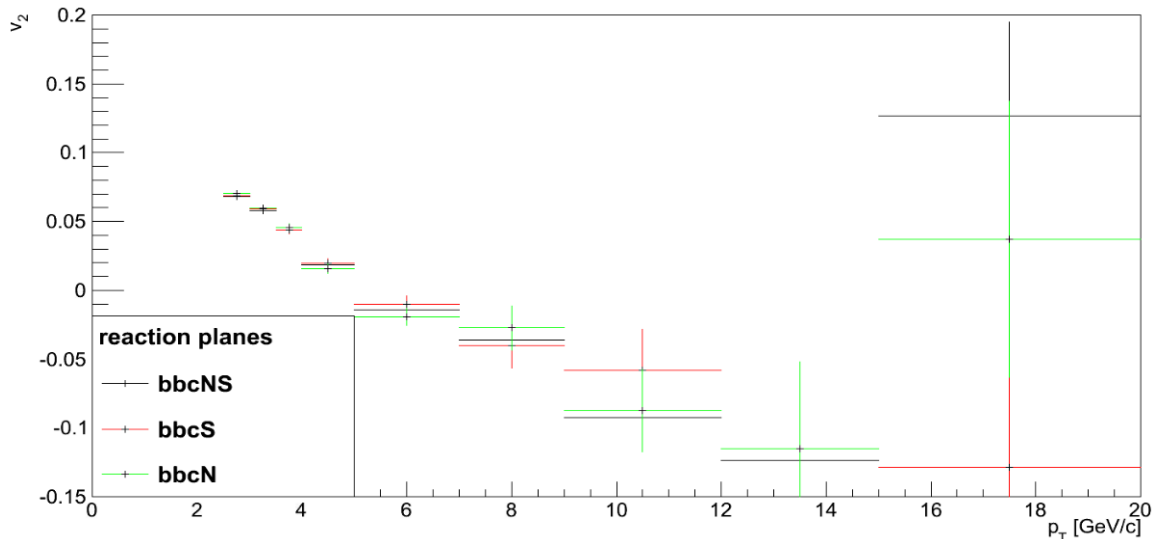
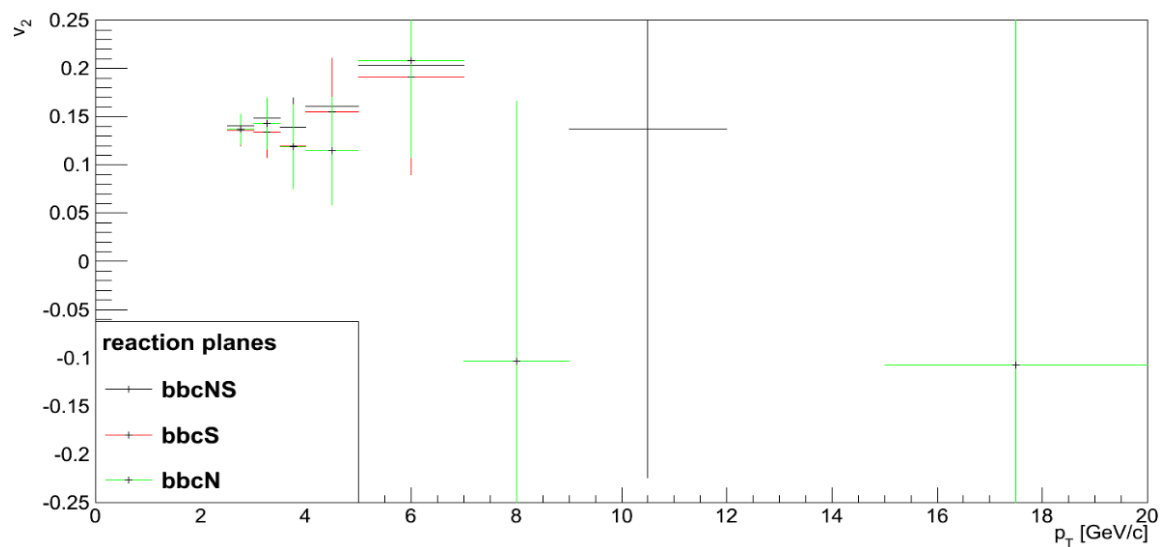
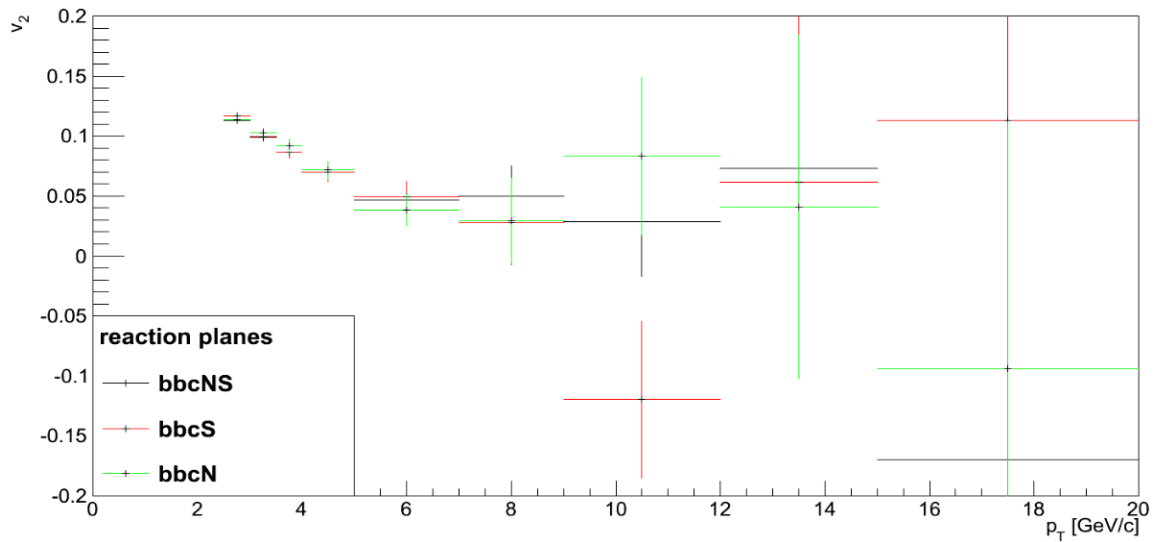
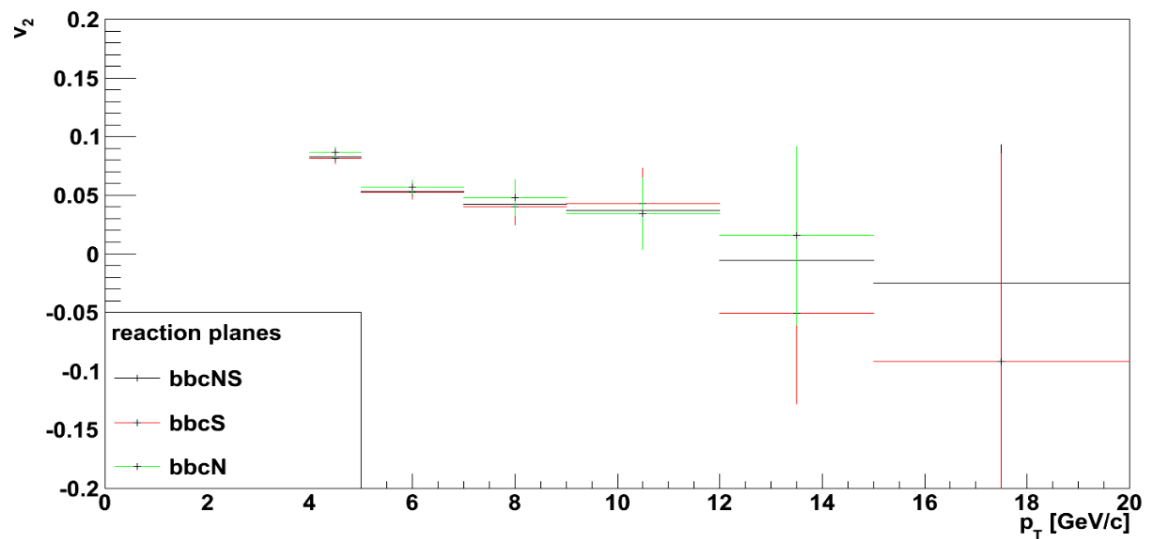
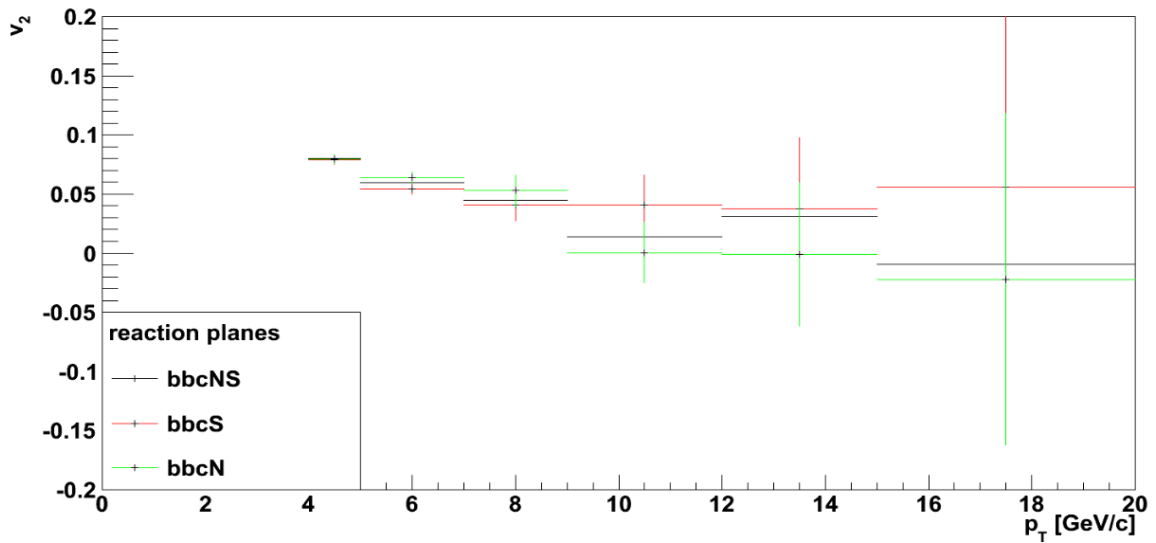


Figure 4.4: Isolated photon  $v_{2\text{effective}}$  versus  $p_T$  for 0-20% centrality.







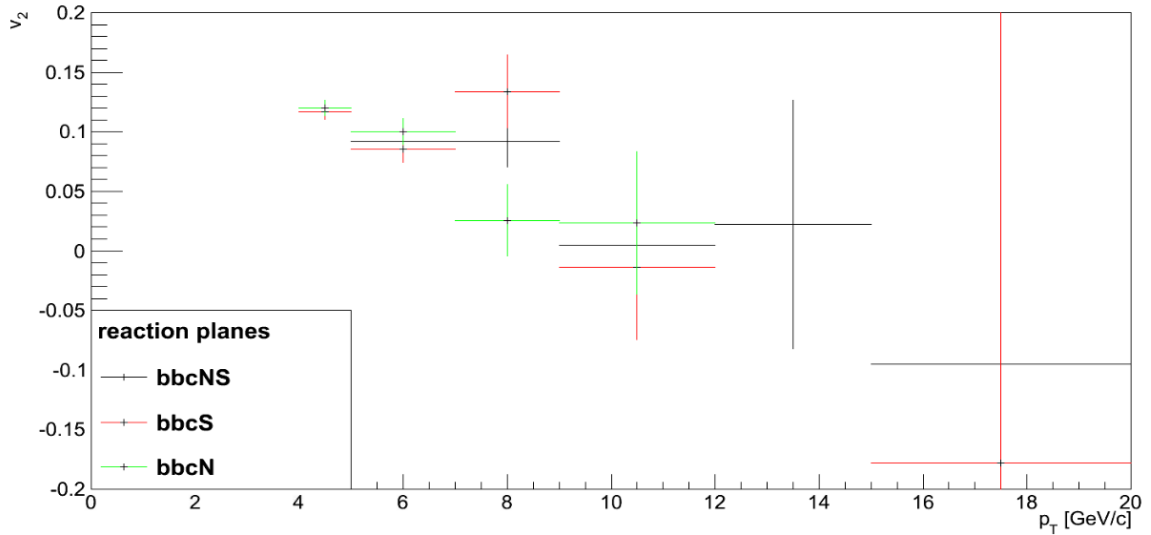


Figure 4.10: Isolated  $\pi^0 v_{2\text{effective}}$  versus  $p_T$  for 40-60% centrality.

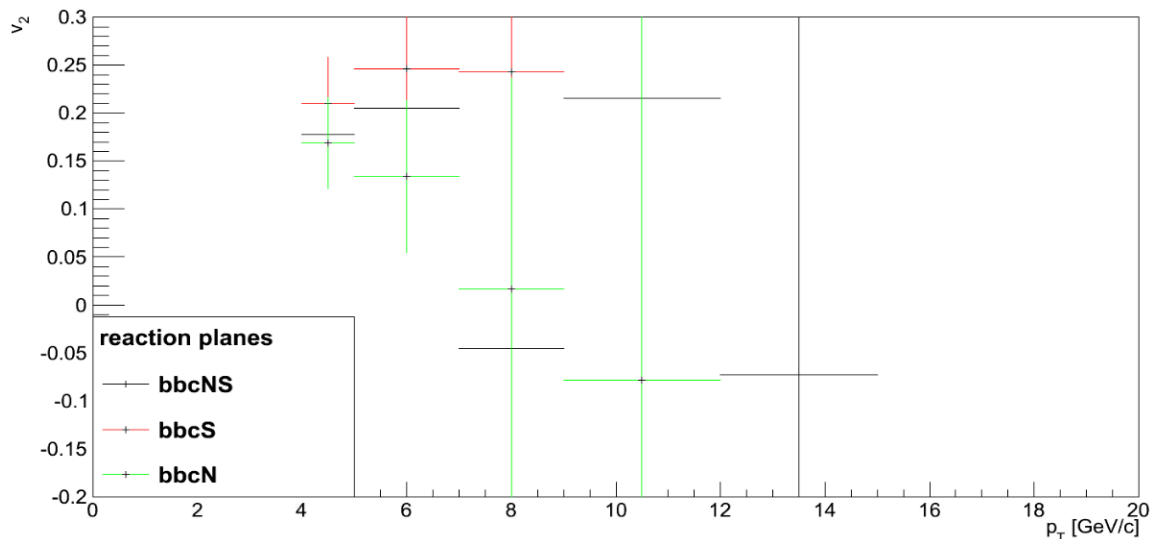


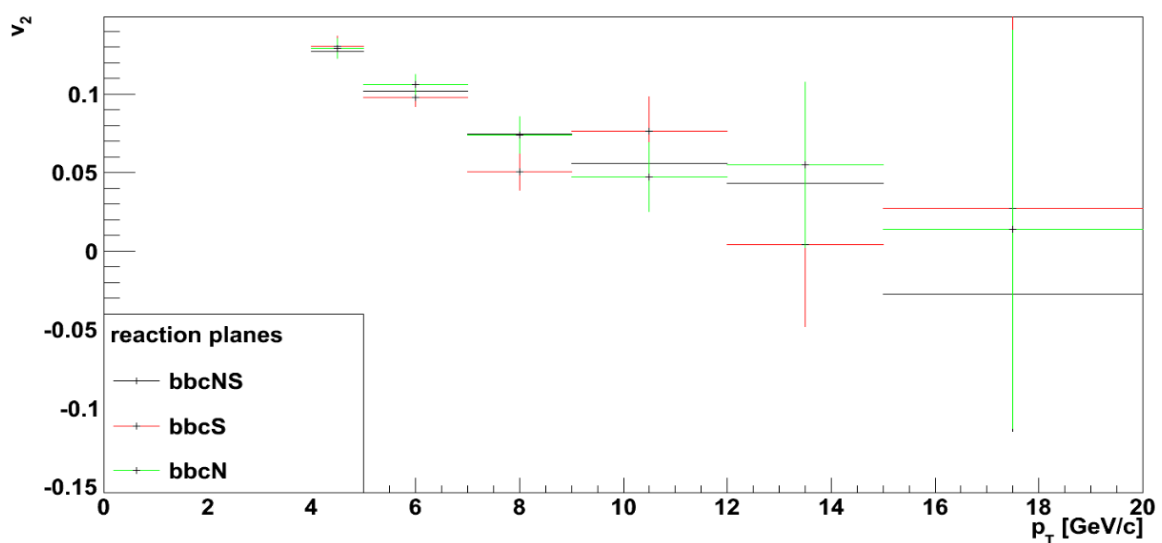
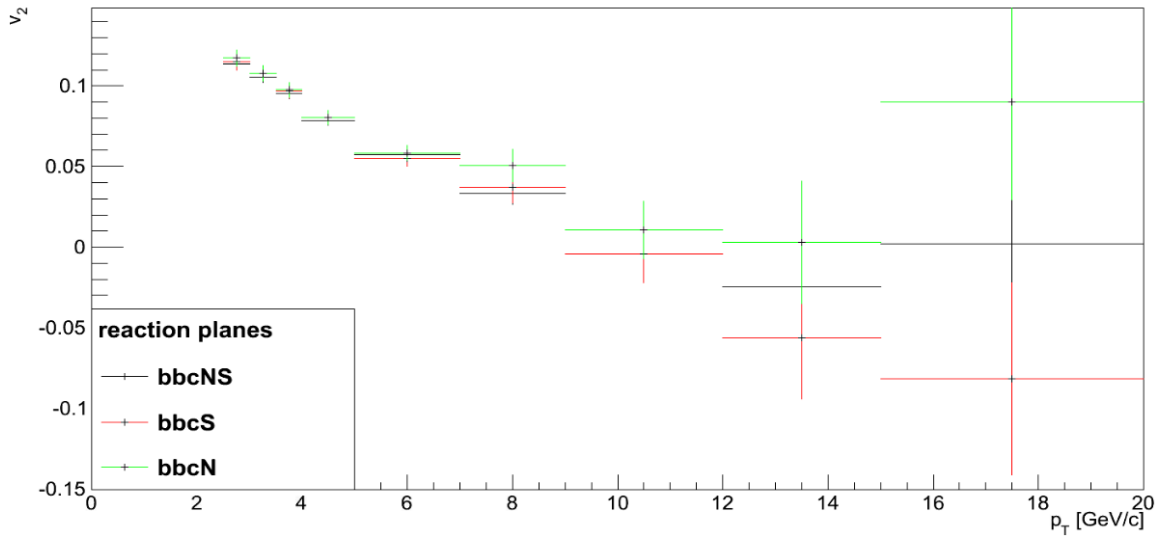
Figure 4.11: Isolated  $\pi^0 v_{2\text{effective}}$  versus  $p_T$  for 60-92% centrality.

These results show a few general trends. The  $v_2$  values decrease as  $p_T$  increases. The trend in the most peripheral events is indiscernible because of the large statistical uncertainties. The error bars are larger on the high  $p_T$  bins because there are a small

number of particles with high  $p_T$ . The reason for this trend is that at low  $p_T$ , hydrodynamic flow contributions dominate. For all  $p_T$  there is small contribution from energy loss, from particles flowing through different parts of the QGP.

One expects the  $v_2$  values of isolated photons to be consistent with zero because the photons originate from the hard scattering that occurs at the beginning of the collision. The isolated  $\pi^0 v_{2\text{effective}}$  is smaller, but finite, than the inclusive  $\pi^0 v_2$  (Figure 1.11). This indicates that energy loss still contributes to the asymmetry at high  $p_T$ , even with the isolation cut. When compared to the most central inclusive photon and  $\pi^0$  measurements (Figures 4.12 and 4.13), one can see that both isolated photons and  $\pi^0$  have smaller  $v_2$  at low  $p_T$  and the  $v_2$  decreases more rapidly as the  $p_T$  increases. This led to the assumption of a reaction plane dependent isolation cut efficiency.

Equation 3.6 describes the measured  $v_{2\text{effective}}$ ; the values in Figures 4.4 - 4.11 are in fact  $v_{2T} + v_{2E}$ , not  $v_{2T}$ . The coefficient  $v_{2E}$  is required in order to find  $v_{2T}$ . A method for finding  $v_{2E}$  is discussed in Section 5.1. It should be stated that these values were obtained by fitting the particle's azimuthal anisotropy (Figure 4.2) to Equation 4.4, not the functional form used with the isolation cut efficiency (Equation 3.6). This is reasonable because both  $v_2$  coefficients have a maximum possible value of 0.5 and are multiplied together so the last term of Equation 3.6 has a negligible effect on the measured  $v_{2\text{effective}}$ . For two particle correlation studies with isolated photons the correct  $v_2$  value is  $v_{2A}v_{2\text{effective}}$ , not  $v_{2A}v_{2T}$  as implied by Equation 1.8.



#### 4.4 Systematic Errors with Resolution Considerations

Elliptic flow coefficients have been measured as a function of  $p_T$  for eight reaction planes. Each reaction plane has a different resolution. The results shown above, Figures 4.4 - 4.11, only show three of these planes. The reason for this is that the resolution corrected RxNP N and RxNP S event planes yield  $v_2$  that are low due to a different resolution that has not been completely corrected for (See Figure 4.14). They should be closer to the other points.

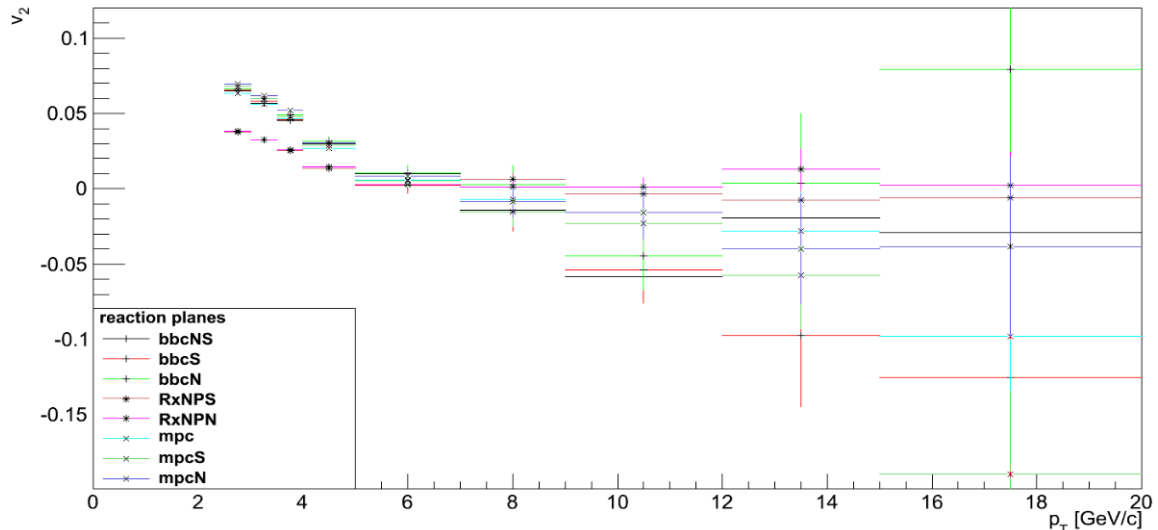


Figure 4.14: Resolution corrected  $v_2$  versus  $p_T$  for isolated photons with 0-20% centrality for eight event planes. At low  $p_T$ , RxNP N and RxNP S event planes are low compared to the other planes due to a different resolution that has not been completely corrected for.

However, if the ratio of isolated photons'  $v_2$  to inclusive photons'  $v_2$  is taken, it should cancel any resolution correction needed. This is because the resolution correction divides the raw measured  $v_2$  by the resolution. Taking the ratio should determine if there is a problem with the determination of the resolution. The ratio can be seen in Figure 4.15. Now, the RxNP N and S are shifted to match the other planes at low  $p_T$ .

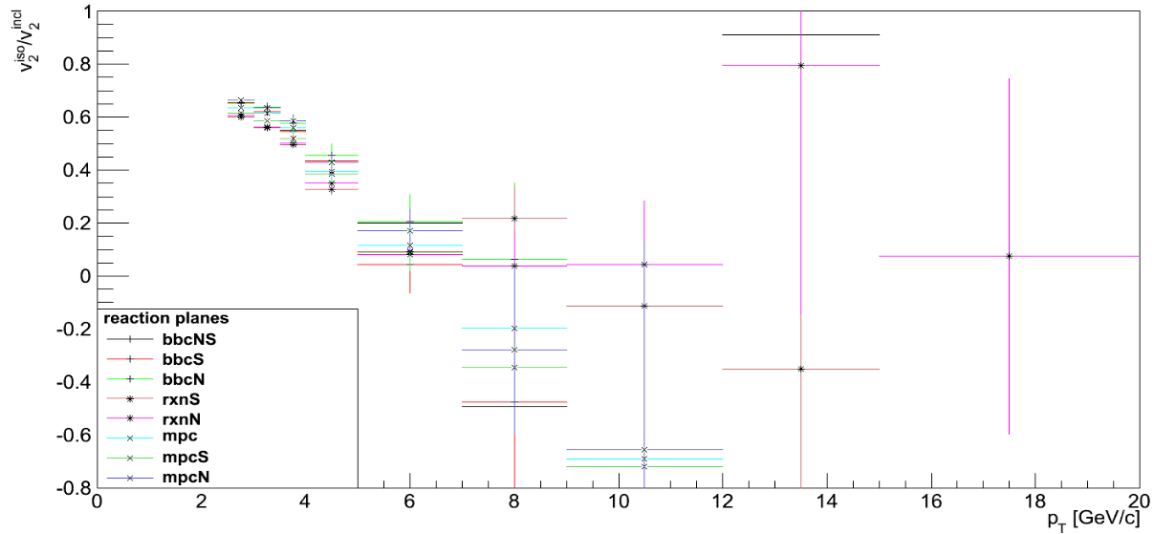


Figure 4.15: Ratio of isolated photon  $v_2$  to inclusive photon  $v_2$  versus  $p_T$  for 0-20% centrality for eight event planes. RxNP N and S are shifted to match the other planes at low  $p_T$ .

Centrality Systematic Error (%)		
$p_T(GeV/c)$	central - mid	mid - periphial
2.5 - 3.5	20	17.5
3.5 - 5.0	33	21
> 5.0	22.5	22.5

Table 4.2: Conservative resolution systematic errors

These systematic errors were determined visually from the spread in the  $v_2$  values in Figure 4.15 and others similar to it for the other centralities. These are conservative error

estimates that should be added to the systematics discussed in Chapter One to get the final systematic error.

## 5 OUTLOOK AND CONCLUSIONS

In order to get the true  $v_2$  value of the isolated photons and  $\pi^0$ 's the cone efficiency must be determined. For the isolated photons it should be close to zero because most of the isolated photons are direct photons. For  $\pi^0$  it may be different because of the jet fragmentation process. In the following Chapter, a method for determining the true  $v_2$  from  $v_{2\text{effective}}$  and  $v_{2E}$  is described, initial measurements of higher order flow coefficients are discussed, and final conclusions are drawn.

### 5.1 Isolation Cut Efficiency

In order to measure  $v_{2E}$ , the cone's energy as a function of  $\Delta\phi$  is measured. Then, the  $\Delta\phi$  bins are projected onto the energy axis. Figure 5.1 shows the cone energy projections for cones that are in the event plane,  $\Delta\phi \approx 0$  (blue points), and out of the event plane  $\Delta\phi \approx 1.25$  (green points). This figure is similar to Figure 3.8 but with measured cones instead of simulated cones. The event plane used in Figure 5.1 is BBC NS for 20-40% centrality. The red line is the value used for  $E_{\text{threshold}}$  and was determined using Equation 4.2 with  $E_\gamma = 2.5$  GeV and the parameters for centrality 20-40% given in Table 4.1. The reader should also be reminded that cones from 0 to  $E_{\text{threshold}}$  are isolated and are used to find the isolation cut efficiency.

The efficiency is determined by taking the ratio of the total integral to the integral from 0 to  $E_{\text{threshold}}$ . This is shown in Figure 5.2. Cones with the lowest efficiency lie in the event plane,  $\Delta\phi \approx 0$ , while the most efficient cones are those that are perpendicular to the event plane,  $\Delta\phi \approx -\pi/2, \pi/2, 3\pi/2$ . The red line is a fit of Equation 3.7, it is shown to guide the eye. In the MC simulation, this distribution is symmetric (Figure 3.9) and Equation 3.7 appears to be a good fit.

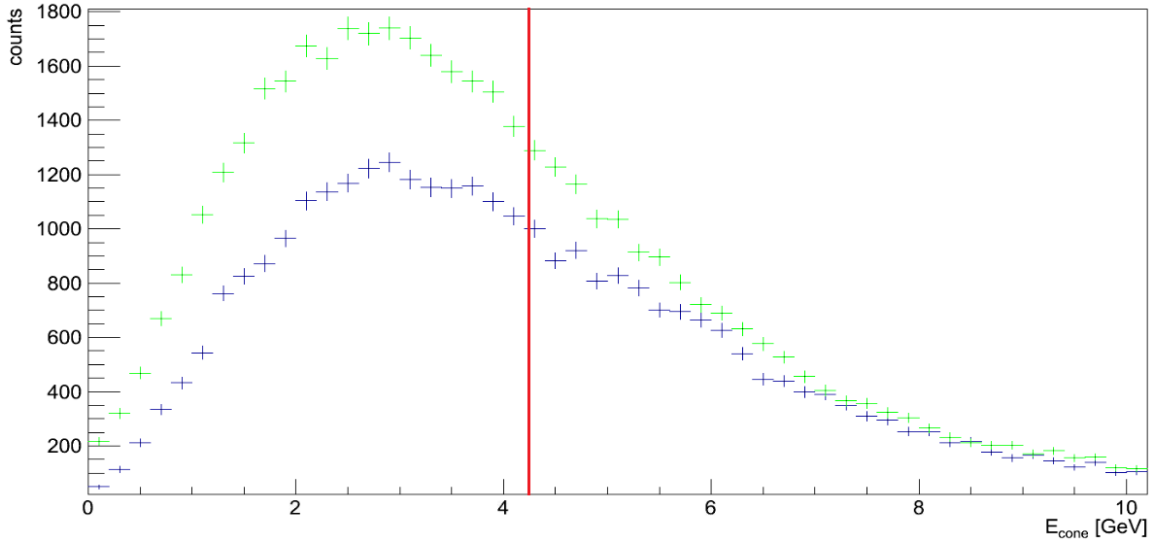


Figure 5.1:  $E_{\text{cone}}$  distributions for cones in (blue curve) and out (green curve) of event plane BBC NS for 20-40% centrality. Ratio of the integral from 0 to the red line to the total integral was taken to find the efficiency. Doing this for the blue curve produces the efficiency  $\Delta\phi$  bin centered around 0. The green curve produces the efficiency  $\Delta\phi$  bin centered around 1.25.

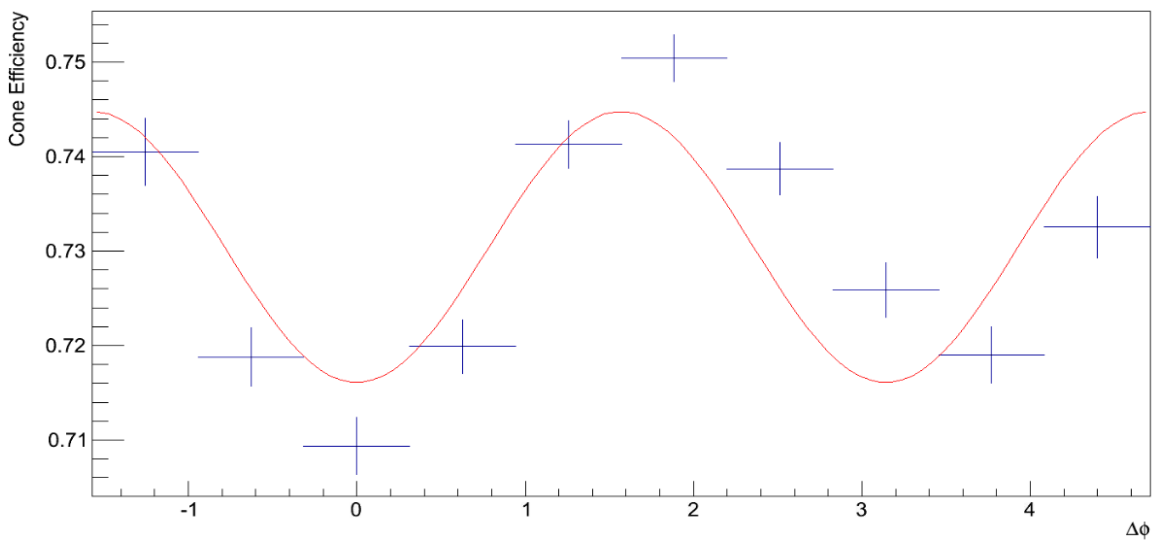


Figure 5.2: Cone efficiency as a function of  $\Delta\phi$ .

The shape of the distribution in Figure 5.2 is what led us to believe that there was a reaction plane dependent isolation cut efficiency. Its shape clearly exhibits a  $1 + 2v_2 \cos(2\Delta\phi)$  like distribution.

The MC simulation has perfect PHENIX azimuthal acceptance, changing this may reproduce the slight asymmetry in the away-side in Figure 5.2. Attempts have been made to reproduce it, they include changing the  $\phi$  acceptance of PHENIX by decreasing the acceptance range as well as only allowing a percentage of particles to be detected. These attempts were not outlandish because the acceptance changes run-by-run; it could easily not have the same limits as the full detectors. There could also be intermittent dead/hot regions that detected particles but they were thrown out in the data selection process. This is reproduced by only accepting a percentage of particles. A combination of these two attempts has been made. A robust method for reproducing this asymmetry more closely in the simulation requires further investigation. To apply this correction to the data, measure  $v_{2\text{effective}}$  then add  $v_{2E}$  to obtain the true  $v_2$ .

## 5.2 Measurement of Higher Order Flow Harmonics

The measurements presented in this thesis can be extended to include higher order flow harmonics. The results in this thesis have been only to second order, thus only  $v_2$  has been considered. Including the third order in the two-particle correlation function would make it more accurate which would in turn make all of the measurements that rely on it to be more accurate. Initial measurements of  $v_3$  have been made for inclusive photons (Figure 5.3) and  $\pi^0$  (Figure 5.4) for all nine reaction planes. These measurements are not resolution corrected. These  $v_3$  flow coefficients should be smaller than the  $v_2$  coefficients but they should be larger than what is shown here. The size of the difference is consistent with expectations for the resolution correction.

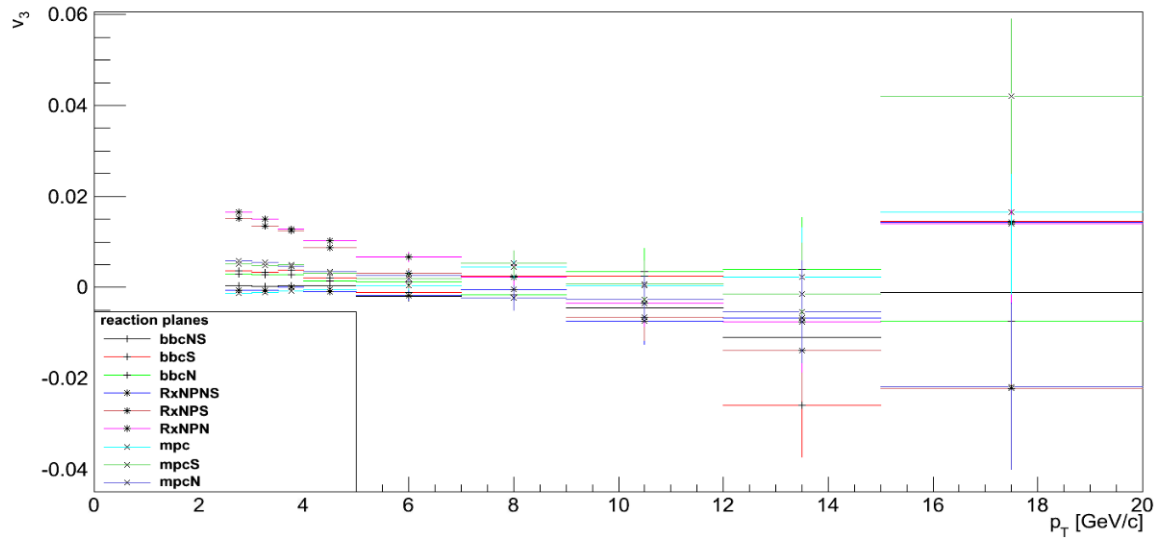


Figure 5.3: Triangular Flow coefficients verses transverse momentum for 20-40% centrality inclusive photons for 9 event planes.

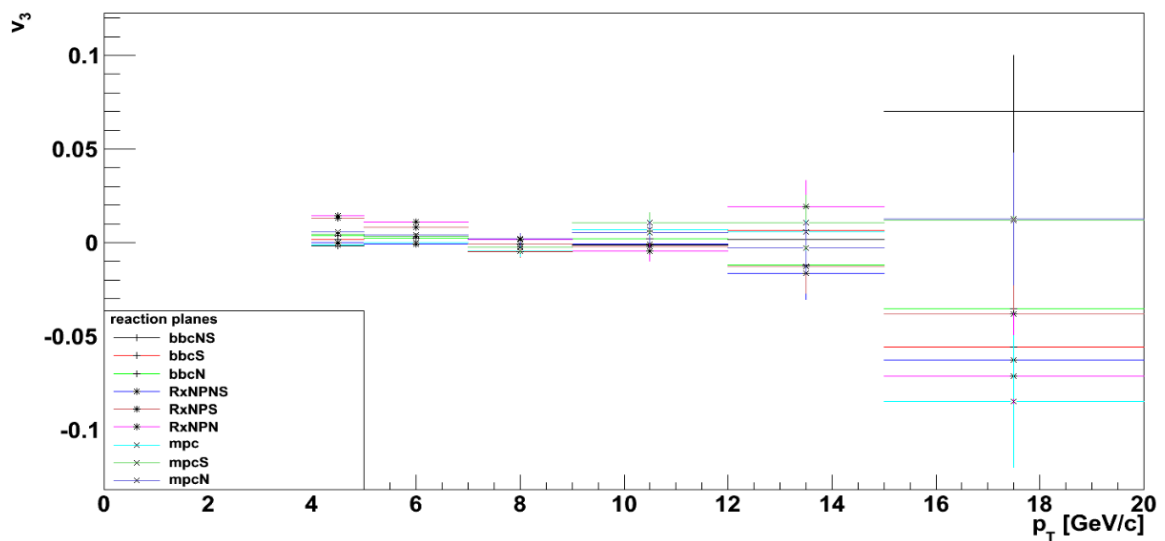


Figure 5.4: Triangular Flow coefficients verses transverse momentum for 20-40% centrality  $\pi^0$  for 9 event planes.

### 5.3 Different Collision Systems

The measurements presented here were from Au+Au collisions at  $\sqrt{s_{NN}} = 200$  GeV. They can be extended to any PHENIX data, seen in Table 2.2. Elliptic flow measurements have been carried out on the Cu+Cu at  $\sqrt{s_{NN}} = 200$  GeV, but not for isolated photons [6]. The isolation cut method used in this thesis must be reformulated for Cu+Cu collisions because the multiplicity is lower than Au+Au collisions.

### 5.4 Final Words

In this thesis we derived the general effect, for single and two-particle azimuthal asymmetry, of a reaction plane dependent efficiency that is harmonic with 2nd-order asymmetry. We also showed that an isolation cut, like those used in direct photon identification where the energy summed inside an angular cone and cut if greater than a threshold energy, will result in such a reaction plane dependent efficiency. Along with these derivations, measurements of isolated photon and  $\pi^0 v_{2\text{effective}}$  values in four centralities of  $\sqrt{s_{NN}} = 200$  GeV Au+Au collisions. The data was collected by PHENIX at RHIC. Once raw  $v_2$  values were determined, they were corrected using a resolution factor that depends on the reaction plane.

The derivations involving the reaction plane dependent efficiency were verified using a Monte Carlo program and show that the measured  $v_{2\text{effective}}$  values that should be used as the  $v_2$  coefficient in the unmodified two particle correlation function (Equation 1.8). They also show that using the usual event plane method to determine the azimuthal asymmetry parameter  $v_2$  will be sensitive only to  $v_{2\text{effective}}$  which includes the sum of true  $v_2$  and the  $v_2$  of the isolation efficiency, which is generally negative. Hence, the measurements of  $v_{2\text{effective}}$  are generally smaller, even reaching negative values, than those previously observed for photons and  $\pi^0$ . Measuring the true isolated photon and  $\pi^0 v_2$  requires finding the efficiency  $v_2$ . A method for finding the efficiency  $v_2$  was presented. Future work

includes incorporating higher order flow harmonics in the derivations and measurements of Au+Au collisions as well as other PHENIX data sets.

## REFERENCES

- [1] J. Beringer *et al.* (Particle Data Group), Phys. Rev. **D86**, 010001 (2012).
- [2] S. Bushwick, “How Low Can RHIC Go?”  
<http://www.bnl.gov/newsroom/news.php?a=21870> (2010), accessed: 2014-08-11.
- [3] CERN, “Heavy Ions and Quark-Gluon Plasma,”  
<http://home.web.cern.ch/about/physics/heavy-ions-and-quark-gluon-plasma>,  
accessed: 2014-08-11.
- [4] RHIC, “The Physics of RHIC,” <http://www.bnl.gov/rhic/physics.asp>, accessed:  
2014-08-11.
- [5] A. M. Poskanzer and S. A. Voloshin, Phys. Rev. C **58**, 1671 (1998).
- [6] A. Adare *et al.* (PHENIX Collaboration), Phys. Rev. Lett. **98**, 162301 (2007).
- [7] S. S. Adler *et al.* (PHENIX Collaboration), Phys. Rev. C **75**, 024909 (2007).
- [8] J. Adams *et al.* (STAR Collaboration), Nucl.Phys. **A757**, 102 (2005),  
arXiv:nucl-ex/0501009 [nucl-ex].
- [9] N. Rivelis, *Direct Photon - Hadron Correlations Measurement in Au+Au Collision at Nucleon Center-Of-Mass Energy of 200 GeV With Isolation Cut Methods*, Ph.D. thesis, Ohio University (2014).
- [10] K. Miki, *Azimuthal Anisotropy Measurement of Neutral Pion and Direct Photon in  $\sqrt{s_{NN}} = 200\text{GeV}$  Au + Au Collisions at RHIC-PHENIX*, Ph.D. thesis, University of Tsukuba (2009).
- [11] E. Richardson, *Elliptic flow at forward rapidity in  $\sqrt{s_{NN}} = 200\text{ GeV}$  Au+Au Collisions*, Ph.D. thesis, University of Maryland, College Park (2012).
- [12] “An Introduction to PHENIX: Detectors,”  
<https://www.phenix.bnl.gov/phenix/WWW/intro/detectors/index.html>, accessed:  
2014-08-11.
- [13] T. Nakamura, “Introduction to PHENIX Beam Beam Counter (BBC),”  
[https://www.phenix.bnl.gov/phenix/WWW/intro/detectors/focus/focus\\_bbc.pdf](https://www.phenix.bnl.gov/phenix/WWW/intro/detectors/focus/focus_bbc.pdf)  
(2002), accessed: 2014-08-11.
- [14] M. Chiu *et al.*, “RHIC Zero Degree Calorimeter,”  
[https://www.phenix.bnl.gov/phenix/WWW/intro/detectors/focus/focus\\_zdc.pdf](https://www.phenix.bnl.gov/phenix/WWW/intro/detectors/focus/focus_zdc.pdf),  
accessed: 2014-08-11.
- [15] S. Afanasiev *et al.* (PHENIX Collaboration), Phys. Rev. C **80**, 024909 (2009).

- [16] M. Chiu *et al.*, “The electromagnetic calorimeter,”  
[https://www.phenix.bnl.gov/phenix/WWW/intro/detectors/focus/focus\\_emc.pdf](https://www.phenix.bnl.gov/phenix/WWW/intro/detectors/focus/focus_emc.pdf)  
(2003), accessed: 2014-08-11.